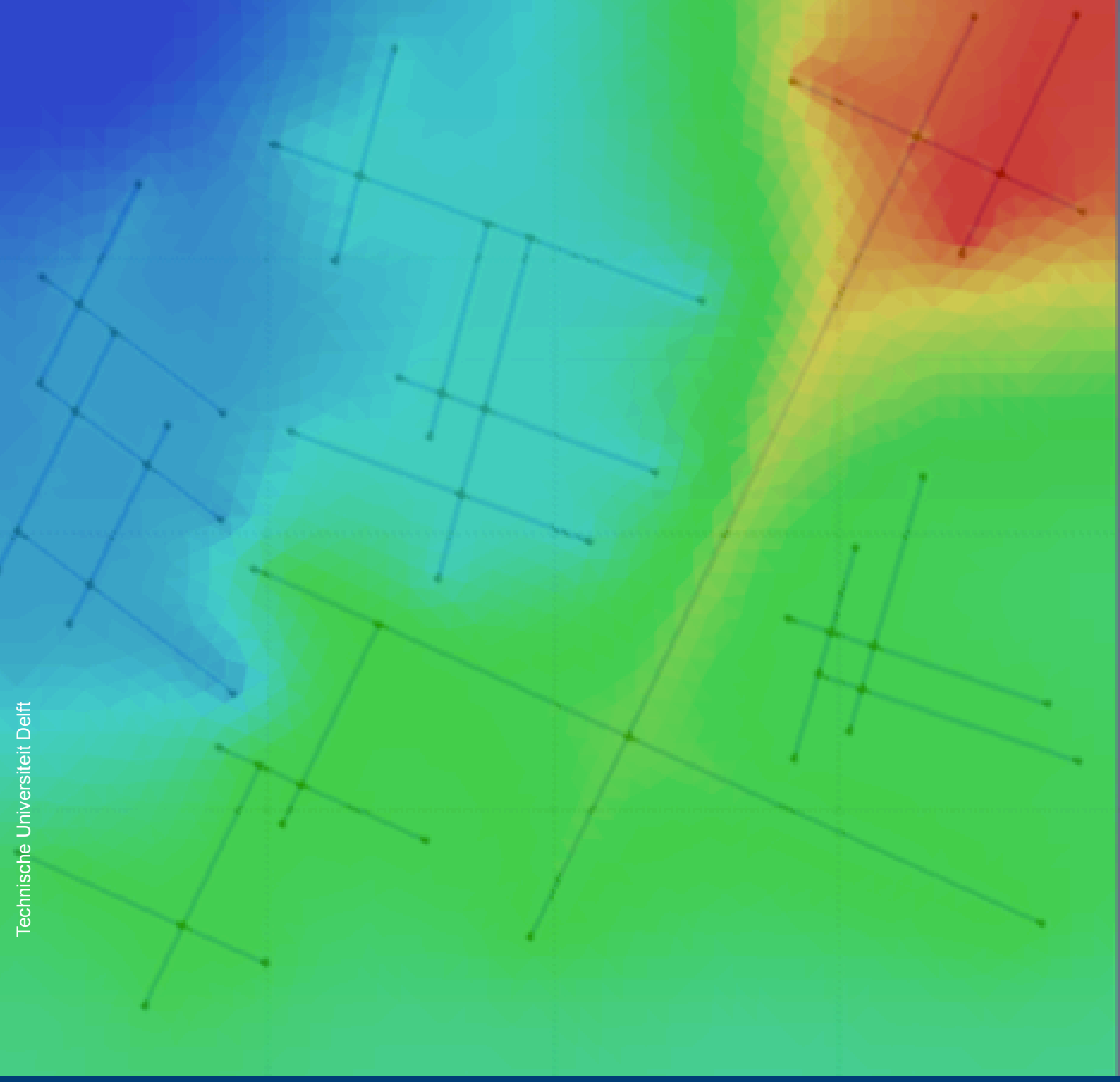

Technische Universiteit Delft

Multiphase flow in tight formations

Ibrahim Mikati

TU Delft

Multiphase flow in tight formations

by

Ibrahim Mikati

to obtain the degree of Master of Science

at the Delft University of Technology,

to be defended publicly on Tuesday March 27, 2018 at 16:00.

Student number:	4514025	
Thesis advisor	Prof. Dr. Denis V. Voskov,	TU Delft, supervisor
Thesis committee:	Dr. Longlong Li,	TU Delft
	Dr. Auke Barnhoorn,	TU Delft
	Prof. Bill Rossen,	TU Delft

An electronic version of this thesis is available at http://repository.tudelft.nl/.

TU Delft

Acknowledgements

Going back to studying after nearly seven years of work was always going to be a challenging experience. Fortunately, I was lucky enough to be surrounded by such a supportive and friendly group of people and I would like to take this opportunity to express my gratitude.

I would like to thank Dr. Denis Voskov for all the support and guidance over the last year. I have learned a lot from him, both as a technical supervisor but also, more importantly, as a person. His calm and patience in the face of challenges inspired me to move forward.

I would also like to thank Longlong Li, for his help with understanding compositional simulators and implementing all the necessary changes, and Mark Khait for his support with AD-GPRS.

I am also grateful for all the friendships made here in beautiful not-so-sunny Delft. To Diego, Raul, Andrea, Ben, Ayla, Ghina, Ali, Huzefa, Roberto, Christian, Thomas, Luc, Ruud, Gabriella, Irene, Prashanth, Timothy....Thank you for keeping me young(ish) at heart.

Finally, I would have never had this opportunity to begin with if it weren't for the continuing support of my family. To my family-Hussein, Afaf, Victoria, Hala, Sarah and Tarek-I love you all and I admire you deeply.

Ibrahim Mikati
Delft, March 2018

Abstract

Given the substantial growth of the shale industry over the last decade, understanding flow in confined spaces will play a primordial role in the future of the upstream petroleum sector. Most compositional simulators are designed for standard (unconfined) reservoirs. Additional physical phenomena occurring in confined spaces such as capillary pressure, diffusion and adsorption are not taken into account. Moreover, most studies conducted on this topic only focus on shale gas, without regards to the presence of a liquid phase. This thesis focuses on the effects of capillary pressure on a multiphase flow and describes the modified production profiles.

Recent studies have shown that elevated capillary pressure in confined spaces modifies the phase behavior of the hydrocarbon mixture, namely causing a reduction of the bubble point, which in turn affects the oil density and viscosity. These modifications will alter well production dynamics.

Standard compositional simulators couple a mass balance equation with conservation laws and thermodynamic equilibrium, which comes in the form of a nonlinear constraint describing the equality of chemical potentials. This research work replaces the last condition with a modified K-value constraint. The K-value is simply the ratio of a component's composition in its vapor phase to its liquid phase. The latter is specific to the pressure, temperature and the hydrocarbon sample's molar composition; and is derived from equations of state (EOS) which are employed to describe the phase behavior of a system. Capillarity is introduced in the K-value by adding the Parachor model, which determines the interfacial tension and the Laplace equation to the EOS derivation.

The modified K-values are incorporated into Stanford's Automatic Differentiation General Purpose Research Simulator (ADGPRS) based on a fully implicit approach. Other necessary modifications were made to include the effects of heterogeneity in the system. Simulations were ran in both simple one-dimensional reservoirs and more complex fractured models depicting fractured shale reservoirs and compared to the production results generated by standard compositional model.

Contents

List of Figures

List of Tables

Nomenclature

δ_{ji}	Binary interaction coefficient between components i and j	$-$
χ_i	Parachor coefficient of component i	$-$
λ_j	Mobility of phase j	$-$
μ_g	Viscosity of gas	$Pa.s$
μ_o	Viscosity of oil	$Pa.s$
μ_w	Viscosity of water	$Pa.s$
ϕ	Porosity	$-$
ρ_g	Density of gas	kg/m^3
ρ_o	Density of oil	kg/m^3
ρ_w	Density of water	kg/m^3
σ_i	Interfacial tension of component i	dyn/cm
φ	Fugacity coefficient	$-$
f_c^p	Fugacity of component c in phase p	bar
K	Absolute permeability	$Darcy$
K_i	Equilibrium ratio of component i	$-$
n_c	Number of components	$-$
n_p	Number of phases	$-$
P	Pressure	bar
r	Pore radius	m
S_g	Saturation of gas	$-$
S_o	Saturation of oil	$-$
S_w	Saturation of water	$-$
T	Temperature	K
u_j	Darcy velocity of phase j	m/s
v	Total vapor fraction of mixture	$-$
x_i	Molar fraction of component i in liquid phase	$-$
y_i	Molar fraction of component i in vapor phase	$-$
z_i	Overall molar fraction of component i	$-$

1

Introduction

The oil shale market has played a prominent role within the oil industry in recent times. Application of enhanced oil recovery methods such as fracturing techniques and horizontal drilling made its evolution possible. However, the advent of large-scale shale gas production did not occur until around the beginning of the century when shale gas production became a commercial reality in the Barnett Shale located in north-central Texas.

Globally, 32 percent of the total estimated natural gas resources are in shale formations, while 10 percent of estimated oil resources are in shale or tight formations. Over the last decade, as natural gas producers gained confidence in their ability to profitably produce natural gas in several field in the United States, there has been a proliferation of drilling activity in several other shale formations. According to the latest report of the Energy Information Administration (EIA), dry shale gas production in the United States has increased from 0.3 trillion cubic feet in 2000 to 9.6 trillion cubic feet in 2012, which accounts to 40 percent of U.S. dry natural gas production [6]. Dry shale gas reserves increased to 94.4 trillion cubic feet by year-end 2010, when they equaled 31 percent of total natural gas reserves.

This development of shale resources has had a number of direct effects. Natural gas prices in the US have declined sharply as a result of shale gas exploration. We observe that investments in energy intensive industries in the US have gone up as a result. This economic success, coupled with a greater independence from what is seen as unreliable energy exporting countries, has caused other countries around the world (including China, India, Argentina, Poland, Ukraine, and many others) to explore their own shale formations for their economic viability [5].

Shales reservoirs have more complex features than conventional reservoirs. Despite the recent shale gas revolution in the US, we still posses a very basic understanding of compositional flow in tight confined spaces [8]. Moreover, the debate still lingers on whether the shale revolution will expand worldwide and have a significant impact on energy politics in various countries as in the United States. Fracking remains a hot topic in terms of environmental impact[12], it presents several risks such as groundwater contamination, frac-induced earthquakes, methane pollution...

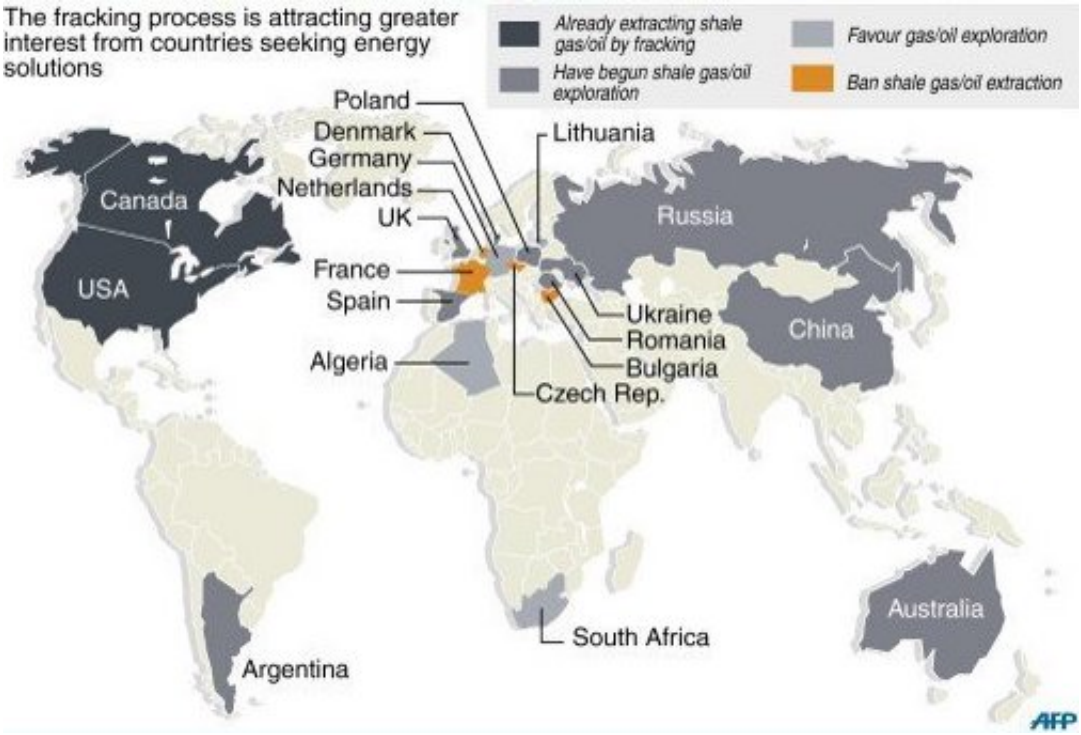

Figure 1.1: Emergence of shale gas and oil [17]

1.1. Shale formations

The most common sedimentary rocks on the Earth's crust are shales, making up over 75% of the clastic fill in sedimentary basins. In contrast to conventional reservoirs, shales have very fined-grained rock texture (dominant grain size < 62 um), low porosity (<10 %), very low permeabilities (nano-Darcy range). These are source rocks with high organic content (> 2 % weight fraction, Total Organic Carbon TOC) that also function as reservoir rocks [10].

Shale formations are known to be very heterogeneous and consist of complex micro structures. Energy dispersive spectroscopy of the shale cross sections indicates that clay, carbonate, quartz, pyrite, and kerogen are the most prevalent components [4]. Pores are observed in both the kerogen and inorganic matrix with the size, shape, and number of pores varying among the shale samples.

Fig.1.2 shows several shale samples extracted from different basins. The dark gray organic material consisting mainly of kerogen, can be seen dispersed within a matrix of inorganic content (light gray to white) comprising of quartz, pyrite and clays. The white arrows point at the organic pores (*organophyllic pores*), it can be noted that the amount of pores in the organic material is much more abundant than the pores in the inorganic content. Several studies also confirmed that organoporosity is the main contributor to the porosity of numerous shale basins [1, 11, 18]. These pores are generated during burial and maturation of organic material. They are dependent on maceral type (e.g. kerogen, bitumen, vitrinite, liptinite...) and thermal maturity. As the thermal maturity of a shale moves from the oil to the gas window, the porosity in the sample sees an increase in the organic part.

The pores in the shale matrix are mainly associated with clay minerals and organic matter and comprehending the controls of these factors on the pore-size distribution is critical to understanding the shale pore network. Although organophyllic nanopores are the most abundant, pores within the inorganic medium can be found as well in three main forms: in-

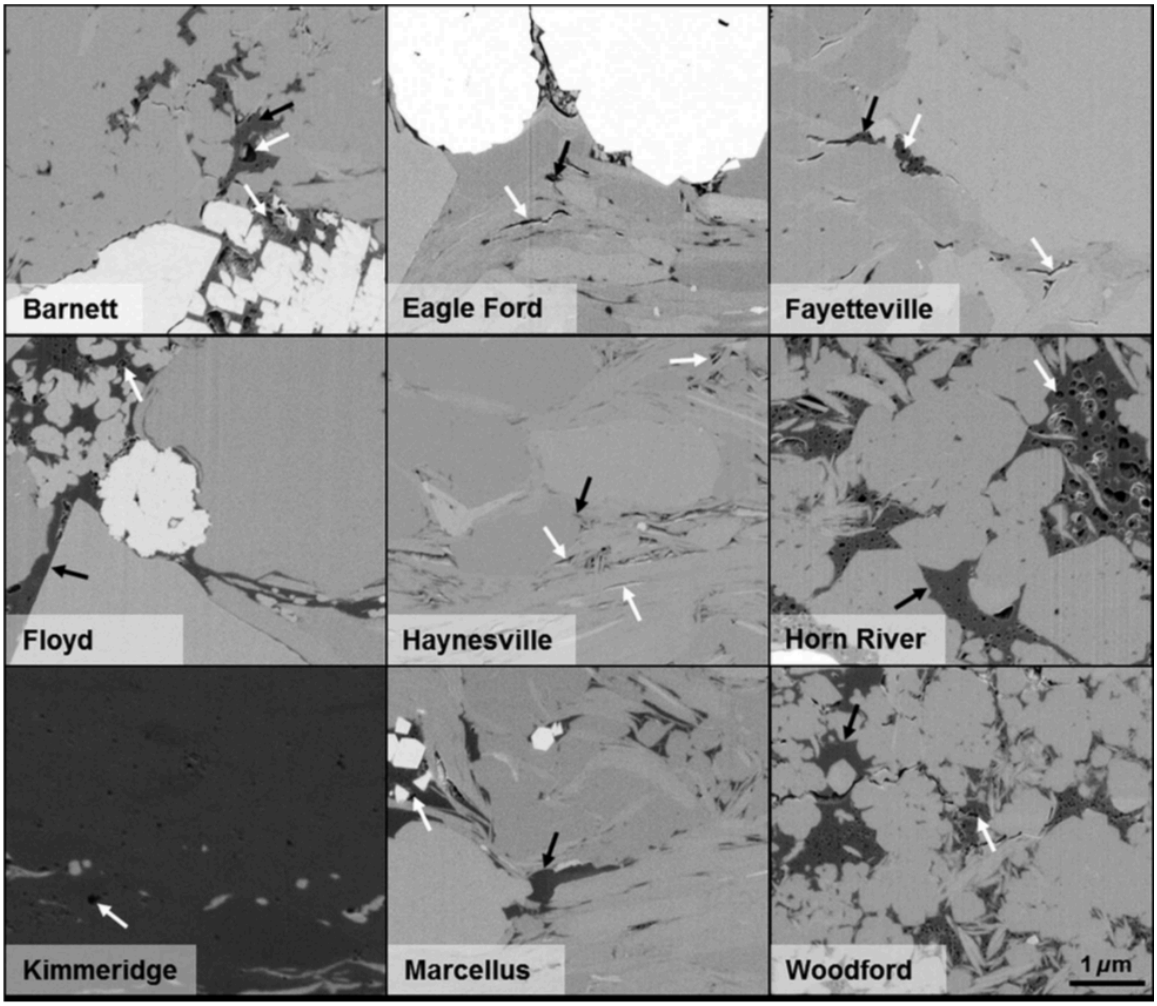

Figure 1.2: Electron images of nine Shale samples [4]

traparticle pores within mineral grains (Fig. 1.3a), microchannels in shale matrix (Fig.1.3c) and microfractures (Fig. 1.3b). Microchannels, which are in the range of hundred of nanometers, are discontinuous and located between bedding planes as results of erosion between the planes or as remains of bioturbation. Microfractures could be natural or induced by drilling, they result primarily from tensile or shear stress applied to the formation.

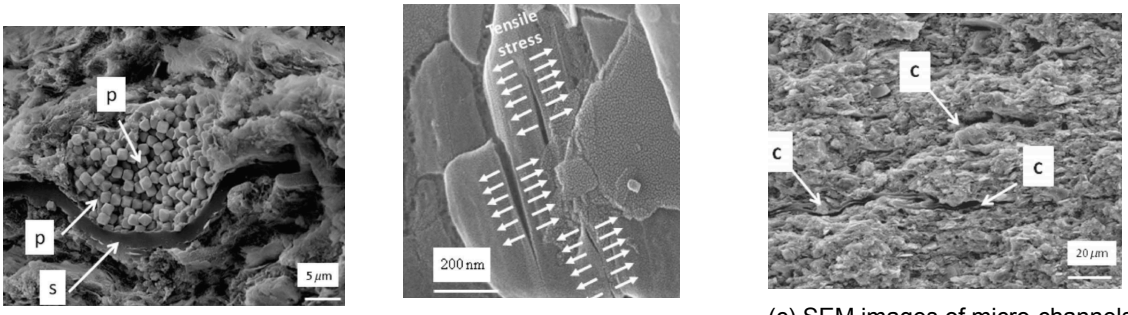

(a) Pores between pyrite crystals

(b) Micro-fractures in inorganic matrix

(c) SEM images of micro-channels in Woodford shale

Figure 1.3: Types of pores in inorganic matrix of shale [18].

The International Union of Pure and Applied Chemistry (IUPAC) classifies pores into the following categories:
1. Micropores: pores with pore size below 2 nm.
2. Mesopores: pores with pore size between 2-50 nm.
3. Macropores: pores with pore size greater than 50 nm.
Nanopores therefore make up a considerable amount of the porous space in shales. The pore throat dimensions of these porosity systems can vary widely, potentially ranging from 10nm to 50μm. The distribution of pore throat sizes will vary reservoir by reservoir as seen in Fig. 1.4.

The two main contributors of permeability are the organic pores in the nano-scale due to their abundance and the micro-fractures and channels due to their interconnectivity. As the hydrocarbon mixture moves from a confined nano-scale media within the organic pores towards the relatively larger micro-fractures, the flow will experience some deviation caused by several physical phenomena. The latter will be discussed in the next section.

1.2. Flow in tight pores

Shale gas reservoirs possess different features from conventional reservoirs, which makes it difficult to study its production behavior. Gas storage in gas shale exists in three major forms: stored as compressed gas in the pore network, adsorbed on the surface of organic material and possibly on clay minerals, and dissolved in liquid hydro-carbon and brine (interstitial and clay-bound), and kerogen [12]. Namely, the main phenomenons resulting from the confined spaces which alter the fluid flow are: elevated capillary pressure, diffusion and adsorption effects.

1.2.1. Capillary Pressure effect

Porosity and pore-size distribution affect the mechanical and elastic behavior of the porous media, as well as the flow of fluid. Tight confined spaces have been known to alter the chemistry of the multiple components of the oil. Confinement can cause shifts in the critical properties of each component within the hydrocarbon mixture. For a very small pore radius, the capillary pressure can be known to be very high. The latter leads to a decrease of bubble

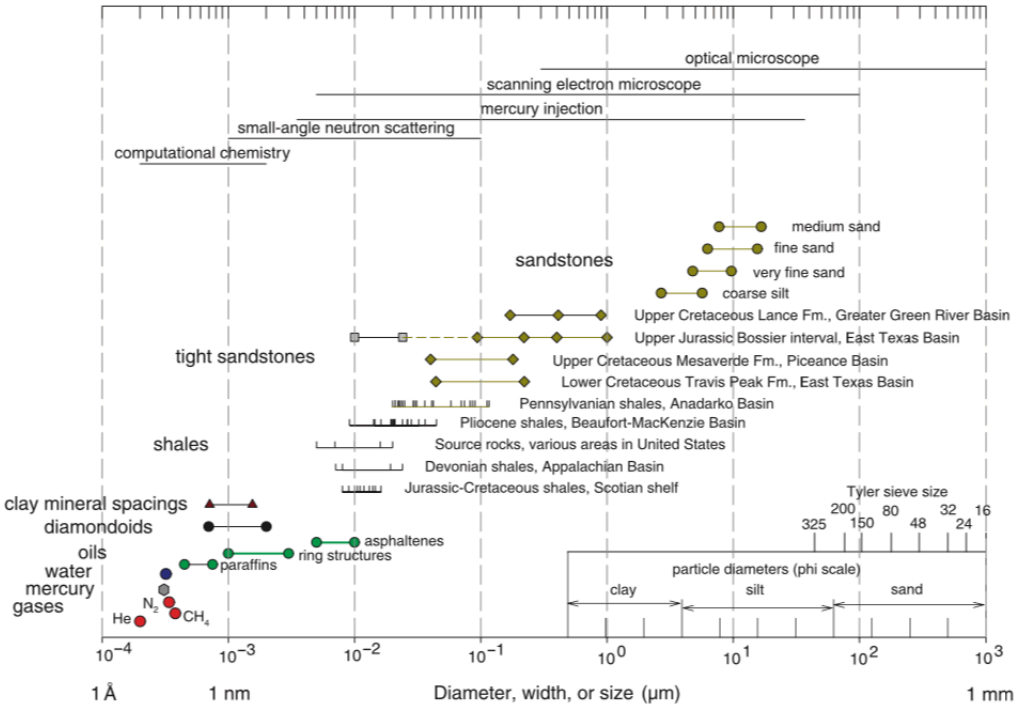

Figure 1.4: Size of molecules and pore throats in siliclastic rocks [14]

point pressure, which in turn reduces the viscosity and the density of the mixture.

Several studies have been made to analyze the effects of very fine pore radii and the consequent large capillary pressures on hydrocarbon properties. In most cases, the same methodology is used, combining standard equations of states (EOS) with Laplace equation and the Parachor model [9, 15, 19].

The Laplace equation is a successful model used to relate to the pressures in vapor and liquid phases from the curved interfaces, which is the boundary of the equilibrium phases. The Parachor model is applied to determine the interfacial tensions of crude oil and gas condensates. Pang and Zuo [16] studied the effect of porous medium on both dew point and bubble point pressures for several condensate and oil systems. They noted that the elevated capillary pressure makes dew point increase in the upper dew point interval and decrease in the lower dew point interval, whereas bubble point always decreases.

Nojabaei and Jones noted that the changes in phase behaviour of hydrocarbons are negligible unless the pore radius is in the order of tens of nanometer [15]. Fig. 1.6a shows that the biggest effects of capillary pressure occur at lower pressures and temperatures for pores in the nano-scale. Moreover, there is no change in saturation pressure or fluid densities at the critical point, where the interfacial tension is zero.

Nojabaei also showed that the lower temperature plays a more significant role in tight pore spaces as seen in Fig. 1.6b. Haider reasserted the results mentioned above and added that the critical properties shift increases as the molecules become heavier (seen in Fig. 1.7). The shift can be neglected for pore sizes larger than 30 nm. The effects of confinement should only be felt in rock matrix and not in fractures, therefore the latter can be considered as regions with infinite pore radius.

This thesis will focus mainly on the effects of confinement in a matrix dominated by nano-pores.

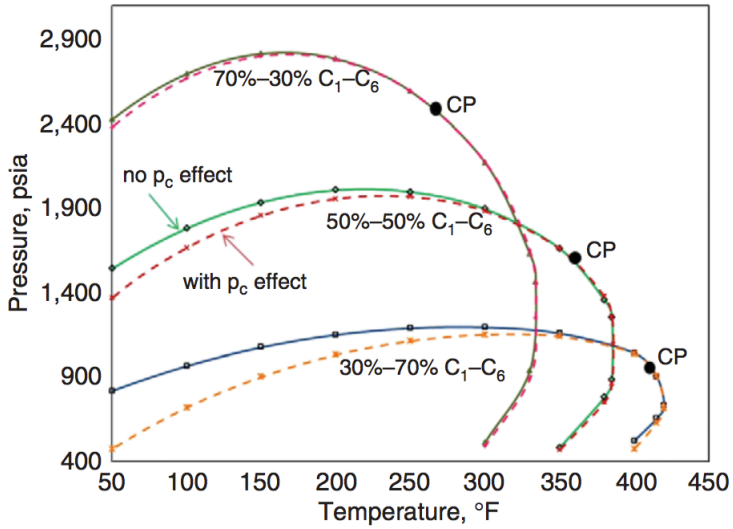

Figure 1.5: Bubble Point reduction due to capillary pressure [15]

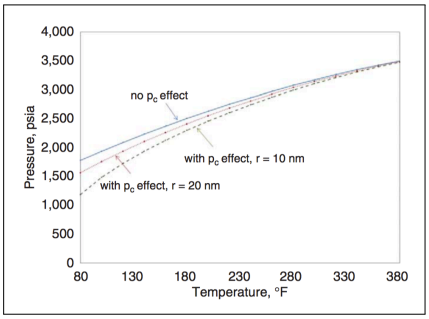

(a) Bubble Point Pressure for Bakken oil [15]

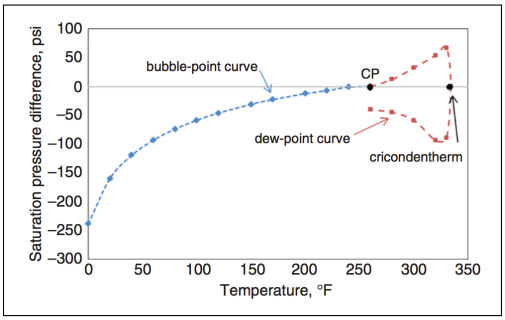

(b) Saturation Pressure differences for 70:30 C1/C6 mixture between standard conditions and pore radius of 10 nm [15]

Figure 1.6: Effects of capillary pressure on Bubble point pressure

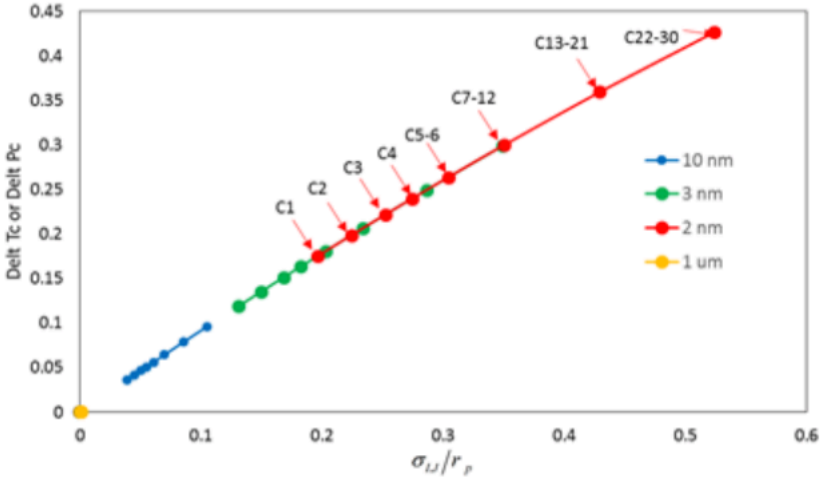

Figure 1.7: Effects of components in Bakken oil [9]

1.2.2. Adsorption

In shale reservoirs, hydrocarbon gas is stored in two ways which are free gas in the pore media and adsorbed gas on the surface of organic material. The organic matter in shale

has a strong adsorption potential due to the large surface area and affinity to methane. The adsorbed gas represents significant quantities of total gas reserves (20-80%) as well as recovery rates, which cannot be ignored in any model or modeling analysis. Past studies have found that methane molecules are adsorbed mainly to the carbon-rich components, i.e. kerogen, correlated with total organic content (TOC) as seen in Fig. 1.9b [20, 21]. As the well is depleted and the pressure decreases, more adsorbed gas will be released from the pores as seen in Fig. 1.8.

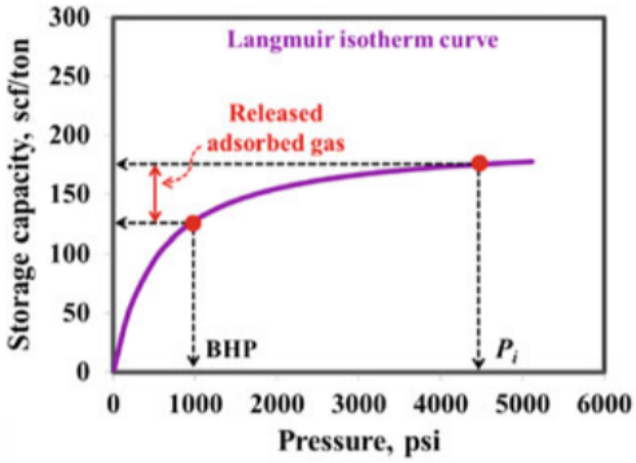

Figure 1.8: Langmuir isotherm

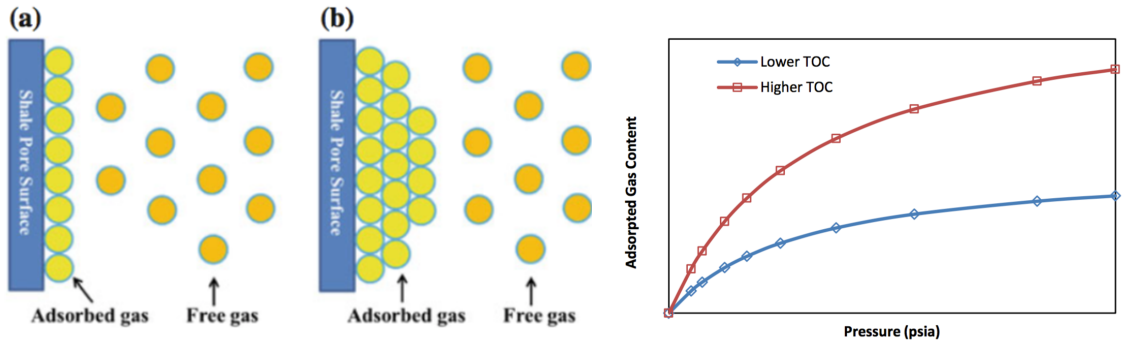

(a) Schematic plot of monolayer and multilayer gas adsorption [21]

(b) Shale adsorbed gas content [20]

1.2.3. Diffusion

Various attempts have been made to model flow in tight gas and shale gas systems. However, there is currently little consensus regarding the impact of molecular diffusion on flow behavior over time in such systems. One known method to determine the type of flow is via the Knudsen number:

$$K_n = \frac{\lambda}{L} \tag{1.1}$$

Where: L is the pore diameter and λ is the mean free path traveled. At low pressures, the hydrocarbon molecules are more likely to collide with the pore wall whereas at higher pressures, they are more likely to collide amongst each other.

At extremely low pore radius, the collisions between the gas molecules and the pore wall are dominant. The regime is defined by non-equilibrium gas flow. There is no comprehensive study on the suitability of various slip models for shale/tight gas flow. Although several

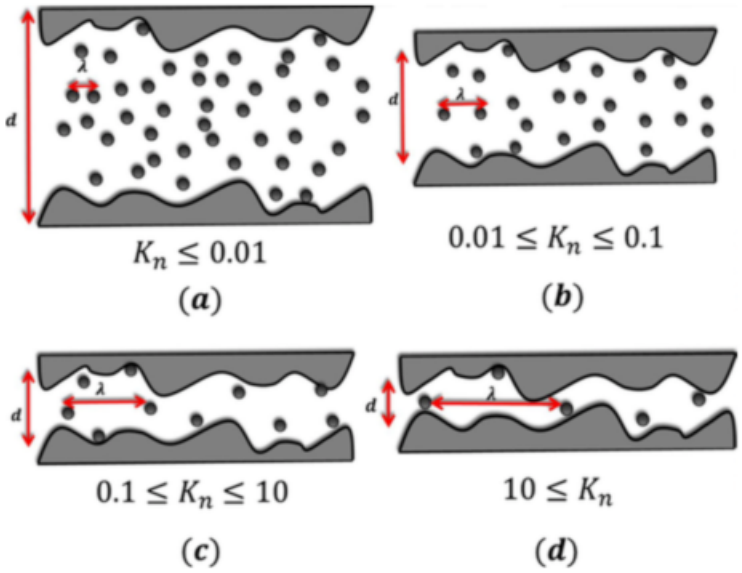

Figure 1.10: Different flow regimes using Knudsen number range, (a) continuum flow, (b)slip flow, (c) transition flow and (d) free molecular flow [13]

studies attempt to explain this phenomena, they are limited to gas flow only (no liquid phase) whereas this thesis will attempt to explain multiphase flow. Therefore, diffusion will not be taken into account in subsequent sections.

1.3. Research description and objective

This thesis is focused around the effects of confinement in both heterogeneous and homogeneous media. Most simulators designed for conventional porous media couple mass balance and transport equations with thermodynamic principles. One of the underlying assumptions is the thermodynamic equilibrium between both vapor and liquid phases for each component. In mathematical terms, it can be written in terms of chemical potentials or, alternatively, fugacities, the equality of which is called equifugacity:

$$f_i^V(y,T,P) = f_i^L(x,T,P), i = 1...N_c \tag{1.2}$$

The above states that the fugacity of one component in its liquid phase is equal to the fugacity in its vapor phase, with the latter being a function of temperature, pressure and molar fractions. One limitation of this equation is that it is dependent on one pressure only. In confined spaces where the capillary pressure is significant, a difference between vapor and liquid pressures can be quite significant.

Another way to approach the thermodynamic equilibrium is to replace the fugacity equation with a corresponding K-value constraint:

$$x_i - K_i y_i = 0, i = 1...N_c \tag{1.3}$$

where K_i is simply the liquid to vapor phase ratio of a specific component, usually assumed to be a function of pressure. This approach is quite accurate when the reservoir composition is far from the critical point.

The aim of this thesis is to develop a modified K-value method taking into consideration the various chemical composition changes inflicted in the nanopores. Using a reliable EOS used

widely in the petroleum industry (Peng-Robinson) coupled with the Young-Laplace equation, a set of K-value incorporating capillary pressure will be generated for a given liquid pressure and pore radius. The latter are added into Stanford's Automatic Differentiation General Purpose Simulator (AD-GPRS), which relies on a fully implicit approach. A model reservoir was built and depleted at pressures above and below bubble point. For each cell, the K-value is extracted and extrapolated beforehand as functions of pressure and pore radius.

Capillary condensation occurs when the vapor phase filling the pores in the micro-scale undergoes a phase transition to liquid (condensed) phase in confined spaces in the range of nanometers. Shale sands, being highly heterogeneous, experience this phenomenon. In one of the simulations studied, we look at the interface between macro and micro scale.

The second shows how K-value tables can be generated and how capillary pressure is included. The third chapter focuses on validating this modified K-value method. Finally, the last chapter shows the simulation results of homogeneous and heterogeneous mediums using this technique.

2

Modified K-value Method

Most compositional simulators are designed for conventional reservoirs. The modifications induced by tight pores and extremely low permeabilities are not taken into account. The objective of this work is to include the effects of capillary pressure into governing equations for conventional compositional problem by introducing a modified K-value into the non-linear system of equations.

2.1. Compositional simulators

One of the governing equations is the mass balance formulation, which dictates that the mass accumulation rate in a system is equal to the net mass influx added to a source term.

$$(Accum.term) = (Netflowofmassinwards) + (sourceterm) + (reactiveterm) \tag{2.1}$$

In our model, the mass exchange is following assumptions of instantaneous thermodynamic equilibrium between different phases and the reactive term can be neglected. In mathematical terms, the general mass balance equation can be written as:

$$\underbrace{\frac{\partial}{\partial t}\left(\phi \sum_p x_{cp}\rho_p S_p\right)}_{accumulation} + \underbrace{div \sum_p x_{cp}\rho_p \vec{u}_p}_{netflowin} + \underbrace{\sum_p x_{cp}\rho_p q_p}_{sourceterm} = 0 \tag{2.2}$$

The subscripts 'c' and 'p' designate the component and phase respectively. p could be either oil, water or gas. The flow of each phase, $\vec{u}_p$, is described by Darcy's law:

$$\vec{u}_p = -K\frac{k_{rp}}{\mu_p}(\nabla P_p - \gamma_p \nabla D) \tag{2.3}$$

Next we assume that only two hydrocarbon phases are present. After spacial discretization, Eq. 2.2 becomes:

$$\frac{V_i \partial}{\partial t}\left[\phi(\rho_o S_o x_c + \rho_g S_g y_c)\right] - \sum_{j \in L} \frac{KA_{ij}}{d_{ij}}\left[x_c \rho_o \frac{k_{ro}}{\mu_o}(P_j - P_i) + y_c \rho_g \frac{k_{rg}}{\mu_g}(P_j - P_i)\right] + \left[x_c \rho_o q_o + + y_c \rho_g q_g\right] = 0 \quad (2.4)$$

where A_{ij} is area of the interface, d_{ij} is the distance between the centers and L is a set of control volumes connected with the control volume i.

Additional local constraints are required to solve the mass balance equation with all its unknowns:

$$\sum_{c=1}^{N_c} x_c = 1, \quad \sum_{c=1}^{N_c} y_c = 1 \quad (2.5)$$

$$S_o + S_g + S_w = 1 \quad (2.6)$$

Finally, as mentioned in the first chapter, a thermodynamic equilibrium condition needs to be satisfied. It is given by:

$$f_c^V(y, T, P_V) = f_c^L(x, T, P_L), \quad c = 1 \ldots N_c \quad (2.7)$$

Or alternatively by:

$$x_c - K_c y_c = 0, \quad c = 1 \ldots N_c \quad (2.8)$$

In Stanford's Automatic Differentiation General Purpose Simulator (AD-GPRS), the K-value is a function of pressure and temperature. In this thesis, the modified K-values will be a function of liquid pressure and pore radius. The latter allows us to include heterogeneity in the system more easily. However, pore radius is not a factor in any of the equations mentioned above. Hence, the first step would be to introduce a link between pore radius and one of the variables in the mass balance equation.

2.2. Introducing a relationship between porosity and pore radius

It is difficult to create a relationship between porosity and pore radius for shale samples since shales can be very diverse. The porosity in shales depends on several factors such as temperature, compaction level, depth, organic content, maturation. An extensive study was conducted on over 40 samples in the Beaufort-Mackenzie basin offshore extracted from varying depths [3]. Combining all the results, a correlation between porosity and pore radius was deduced for the lower porosity samples shown in Fig. 2.1.

From the Fig. 2.1, we note that the higher porosity samples are more scattered since there is more heterogeneity involved there. The trend-line was hence adopted mainly for the lower porosity samples (<10 %) and the following correlation was extracted:

$$r = 0.6317\phi^{1.5135} \quad (2.9)$$

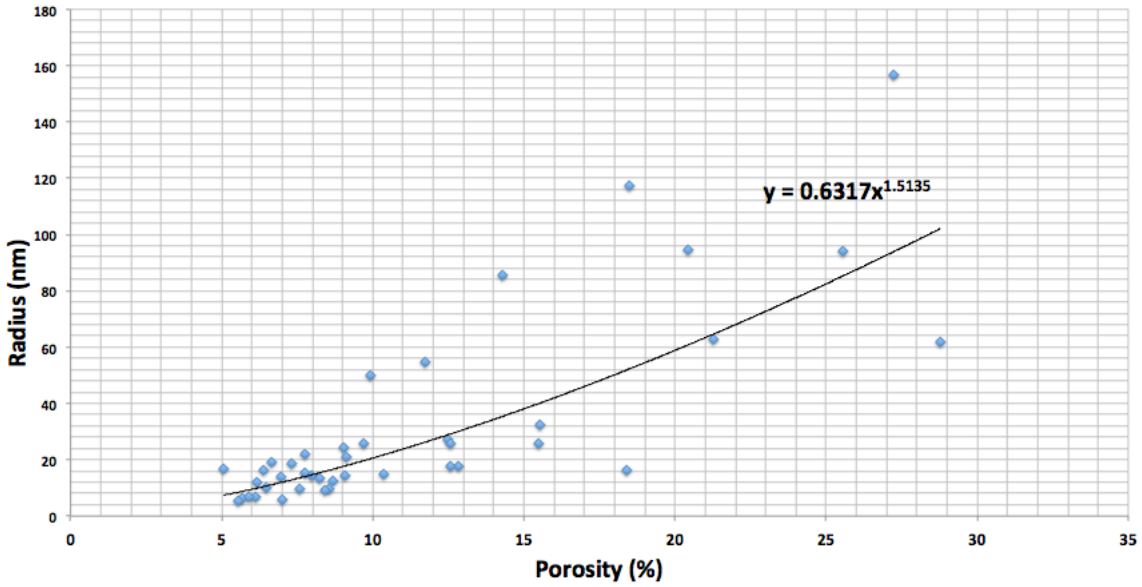

Figure 2.1: Correlation Pore radius-Porosity for Beaufort-MacKenzie basin

2.3. Generation of K values

The following section explains how K-values that incorporate capillary pressure are generated. The K-values are equilibrium ratios specific to each component and are defined as:

$$K_i = \frac{y_i}{x_i} \tag{2.10}$$

The subscript i denotes one component, with y_i and x_i representing the vapor and liquid fractions respectively.

In conventional isothermal compositional simulators, K-values are dependent on pressure. However, the modified K-values for shale medium become a function of liquid pressure and pore radius. The main inputs required for this computation are the pressure, temperature, pore radius, and the molar fractional proportion of each component, z_i. The chemical properties that follow each component are:

- The molar weights M_i.
- The critical pressures and temperatures, $P_{c,i}$ and $T_{c,i}$.
- The acentric factors, w_i.The acentric factor is a measure of the non-sphericity (centricity) of molecules.[2] As it increases, the vapor curve is ”pulled” down, resulting in higher boiling points.
- The parachor coefficients, χ_i used in interfacial tension (IFT) correlation.
- The binary interaction coefficients between components i and j, δ_{ji}.

As a starting point, only one pressure is provided without much knowledge of IFT. $P = P^V = P^L$.[1] Generating modified K-values is done in the following steps:

[1]The upper scripts ’L’ and ’V’ designate liquid and vapor phases respectively.

1. Compute the vapor and liquid fractions of each component, y_i and x_i. This is done by obtaining the vapor fraction of the composition, V, using flash calculation. An initial K-value can be estimated using Wilson's equation.
2. Calculate the gas compressibility factors, Z_i^V and Z_i^L, and subsequently the liquid and vapor fugacities for each component, f_i^L and f_i^V using Equations of state.
3. Update K values as system converges towards equilibrium, $f_i^V = f_i^L$.
   The K values computed so far don't take into account the effects of capillary pressure since the vapor pressure is not calculated yet. The subsequent steps will introduce the necessary modifications
4. Calculate IFT for every component between its liquid and vapor phase using the Macleod and Sugden correlation and consequently, the capillary pressure P_c.
5. Update the Vapor phase pressure P^v for every component.
6. Repeat steps 1 through 3 with the updated vapor pressure until K-values converge.
7. Using the newfound K-value, repeat steps 4 to 6 to update the capillary pressure. Keep repeating until capillary pressure converges towards a value such that $(P_v)_{new} - (P_v)_{old} < \epsilon$ with $\epsilon = 10^{-5}$.

2.3.1. Calculation of vapor and liquid fractions

Initial estimation of K-value

The first step is to compute an estimation of the K-factor using Wilson's equation, where K is given only as a function of pressure and temperature. This correlation is usually limited to low and moderate pressures (up to 3.5 MPa). The acentric factor ω_i is specific to every component. As a result, an initial K-factor will be computed for every component.

$$K_i = \frac{P_{c_i}}{P} exp[5.37(1 + \omega_i)(1 - \frac{T_{c_i}}{T})] \tag{2.11}$$

The above K-value is derived based on Raoult-Dalton's formulation and is not a function of the composition of each phase, only pressure and temperature. The previous assumption is valid only when dealing with ideal substances, and is therefore not entirely accurate in general cases. However it can be used as an initial guess and can be developed further to obtain more accurate K-values. A more rigorous thermodynamic model needs to be then followed to obtain 'real' equilibrium ratios K_i.

Negative flash calculation

Using the initial K-value, both the vapor and liquid fractions of each component can then be deduced. The molar fraction of a component i in the hydrocarbon mixture is equal to the number of moles of i per mole in the vapor phase added to the number of moles of i in the liquid phase:

$$z_i = y_i \upsilon + x_i(1 - \upsilon) \tag{2.12}$$

Using the equilibrium ratio defined in 2.10, we can solve for y_i:

$$y_i = \frac{z_i K_i}{1 + \upsilon(K_i + 1)} \tag{2.13}$$

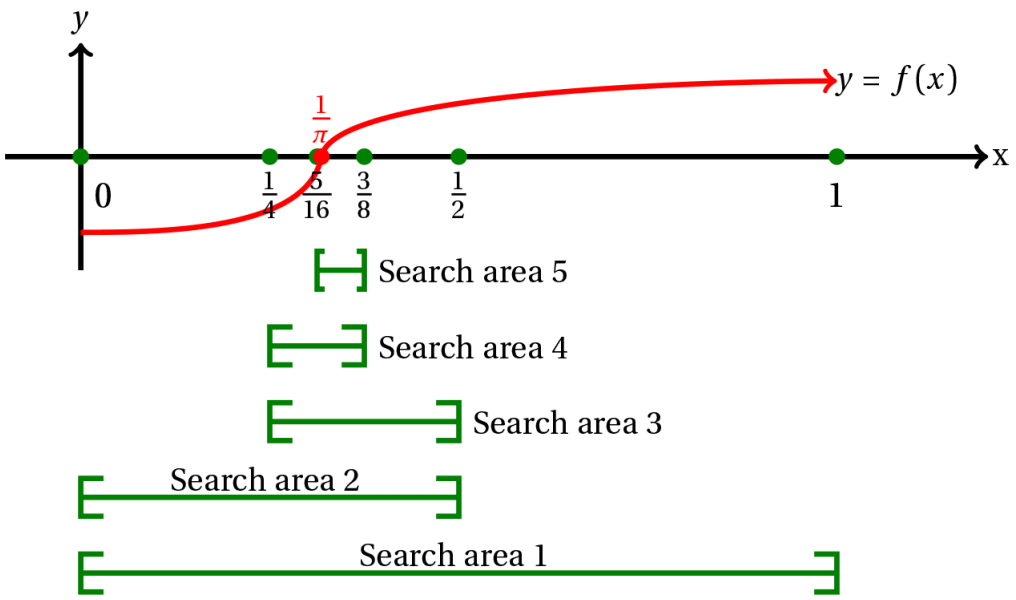

Figure 2.2: Bisection method (source:$http://amsi.org.au/ESA_Senior_Years/SeniorTopic3/3j/3j_2content_1.html$)

Adding the constraint that stipulates that mole fractions must add up to unity $\sum_{i=1}^{n_c} y_i = \sum_{i=1}^{n_c} x_i = 1$, we can deduce the following nonlinear equation:

$$h(v) = \sum_{i=1}^{nc} \left[\frac{z_i(K_i - 1)}{v(K_i - 1) + 1} \right] = 0 \tag{2.14}$$

The equation 2.14 is also known as the Rashford-Rice equation. The vapor phase fraction of the entire composition, v, can then be determined at any given pressure and temperature. In our work, we assume a low-pressure system far from the critical region. Outside these conditions, several complications occur. The inputs provided for this equation are the K values and the molar fractions z specific for each component present within the oil.

Equation 2.14 requires the initial K-value obtained in equation 2.11, from which a solution is reached after several iterations using the bisection method. The objective of the Bisection method is to find a solution(s) to the equation f(x) = 0, where the solution is located within a range [a,b]. An iteration process is built resulting in the convergence of the variable x towards a single value. The method is summed up in Fig. 2.2. In this case, the solution interval is defined by $[\frac{1}{1-K_max}, \frac{1}{1-K_min}]$ relations where K_{min} and K_{max} are the smallest and largest K-values.

Once the solution v, is obtained, the vapor fraction of each component, y_i, can then be determined from 2.13 and subsequently, the liquid fraction is determined via:

$$x_i = \frac{y_i}{K_i}. \tag{2.15}$$

2.3.2. K-value update

Once the vapor and liquid fractions of each component are known, a more accurate K-value can then be deduced using equations of state, based on chemical thermodynamic principles.

Equations of State

Constructing a cubic equation of state requires knowing how the intermolecular forces behave. A proper understanding of the molecular properties gives us a valuation of the macroscopic properties (pressure, temperature). One of the most successful equations is the Van Der Waals equation. Some more recent equations have been designed, but they offer minor variations on the original design. We may write the equation of state as : $Z = 1 + Z_{rep} + Z_{att}$.[2] The final EOS expressed the attractive energy in terms of a parameter which is referred to as a, and the size parameter b. It is given as:

$$P = \frac{RT}{V-b} - \frac{a}{V^2} \quad \text{or} \quad Z = \frac{RT\rho}{1-b\rho} - \frac{a\rho}{RT} \tag{2.16}$$

Since Van Der Waals' proposed formulation, many modifications have been proposed. Peng and Robinson's (1976) [] equation is one of the more widely used in the oil industry. From their part, a semi-empirical correction to Van Der Waals' characterisation of the attractive term with a constant a has been applied with the form $a = a(T, w)$. The Peng and Robinson EOS is given by:

$$Z = \frac{1}{1-b\rho} - \frac{a}{bRT}.\frac{b\rho}{1+2b\rho-\rho^2 b^2} \tag{2.17}$$

where ρ is the molar density and a depends on temperature and the acentric factor. The EOS coefficients a and b were defined as:

$$a = 0.45723553\alpha\frac{R^2T_c^2}{P_c} \quad \text{and} \quad b = 0.0778R\frac{T_c}{P_c} \tag{2.18}$$

$$\alpha = [1 + (0.37464 + 1.54226\omega - 0.26992\omega^2)(1 - \sqrt{T_r})]^2 \tag{2.19}$$

The main reason for the success of the Peng-Robinson equation is that it is primarily applied to Vapor-Liquid equilibria. Since the critical point and the acentric factor ω characterize the vapor pressure fairly accurately, the inclusion of the latter in the EOS gives a good representation of the vapor-liquid equilibria.

In most cases, pressure and temperature are given and standard methods for solutions to cubic equations can be applied. In cubic form, Peng-Robinson can be rewritten as:

$$\boxed{Z_i^3 - (1-B_i)Z_i^2 + (A_i - 3B_i^2 - 2B_i)Z_i - (A_iB_i - B_i^2 - B_i^3) = 0} \tag{2.20}$$

Here, the dimensionless parameters A and B were introduced as:

$$A_i \equiv \frac{a_iP}{R^2T^2} \quad \text{and} \quad B_i \equiv \frac{b_iP}{RT}, \tag{2.21}$$

where the pressure P is relative to each phase. Hence, two compressibility factors will be calculated for every component: one in the vapor phase, Z_i^v, and one in the liquid phase, Z_i^L.

[2] Zrep represents the repulsive interactions whereas Zatt represents the attractive ones.

For multi-compositional mixtures, additional parameters were incorporated to the above EOS. For i components within the mixture, we will have:

$$a_i = 0.45723553\alpha_i \frac{R^2 T_{ci}^2}{P_{ci}} \quad \text{and} \quad b_i = 0.0778R\frac{T_{ci}}{P_{ci}} \tag{2.22}$$

The interactions between the components are included in the following:

$$a_{ji} = (1 - \delta_{ji}) a_j^{0.5} a_i^{0.5}, \tag{2.23}$$

where δ_{ji} is the binary interaction coefficient between components i an j.

The EOS coefficients a_L and b_L for the liquid phase can then be written as:

$$a^L = \sum_j \sum_i x_j x_i a_{ji} \quad \text{and} \quad b^L = \sum_i x_i b_i \tag{2.24}$$

For the vapor phase, the EOS coefficients are:

$$a^V = \sum_j \sum_i y_j y_i a_{ji} \quad \text{and} \quad b^V = \sum_i y_i b_i \tag{2.25}$$

Once the above coefficients are computed, the compressibility factors can be determined from Eq. 2.20 for both phases.

The liquid fugacity,f_i^L, for each component can then be deduced via:

$$ln(\frac{f_i^L}{\mathbf{x_i P^L}}) = \frac{b_i}{\mathbf{b^L}}(Z^L - 1) - ln(Z^L - B) - \frac{A}{2B\sqrt{2}}(\frac{2\sum_j \mathbf{x_j} a_{ji}}{\mathbf{a^L}} - \frac{b_i}{\mathbf{b^L}}) ln(\frac{Z^L + (\sqrt{2}+1)B}{Z^L - (\sqrt{2}-1)B}) \tag{2.26}$$

Likewise, the vapor fugacity,f_i^V, is given by:

$$ln(\frac{f_i^V}{\mathbf{y_i P^v}}) = \frac{b_i}{\mathbf{b^V}}(Z^V - 1) - ln(Z^V - B) - \frac{A}{2B\sqrt{2}}(\frac{2\sum_j \mathbf{y_j} a_{ji}}{\mathbf{a^V}} - \frac{b_i}{\mathbf{b^V}}) ln(\frac{Z^V + (\sqrt{2}+1)B}{Z^V - (\sqrt{2}-1)B}) \tag{2.27}$$

The most notable differences between both values are the pressures and the compositions (highlighted in bold in Eqs 2.26 and 3.15).

Convergence of K-value

We will obtain two separate values for liquid and vapor fugacities per composition. However, one of the fundamental equilibrium properties in thermodynamics requires that fugacities in both phases need to be equal:

$$\boxed{f^L(P_L, T, x_1, x_2, .., x_{nc}) = f^V(P_v, T, y_1, y_2, .., y_{nc})} \tag{2.28}$$

The derivation of the above is described in appendix A.1.

To reach that equality, the K-value needs to be updated in the following manner:

$$K_i^{m+1} = [K_i \frac{f_i^L}{f_i^V}]^m \tag{2.29}$$

The new K-value is fed again into the Rashford-Rice equation 2.14 and the compositions y_i and x_i are updated. Subsequently, the compressibility factors, Z, and the fugacities can be corrected from Eqs. 2.20, 2.26 and 3.15.

The operation is repeated until equilibrium is reached and K values converge for each component. The resulting K-values are more accurate values than the ones computed using Wilson's equation and are functions of pressure, temperature and composition of the separate phases. However, the effects of capillarity are not included as of yet. Only one pressure is provided (Liquid pressure).

2.3.3. Effects of Capillary Pressure

The next segment explains how capillary pressure is included in the converged K-values.

Given the initial pressure P_L and the compositions of the phases, the interfacial tension (IFT) can be deduced using the Macleod-Sugden formulation:

$$\sigma_i = [\sum_i^{Nc} \chi_i (x_i \rho_i^L - y_i \rho_i^V)]^4 \tag{2.30}$$

Capillary pressure is then calculated on the basis of the Young-Laplace equation:

$$P_{c,i} = P^V - P^L = \frac{2\sigma_i}{r} \tag{2.31}$$

The vapor pressure P_v can then be updated for a specified pore radius for each component. Subsequently, the phase compositions, x_i and y_i, need to be re-calculated, along with the compressibility factors and the fugacities. The corrected K-value will then incorporate capillary pressure. The above procedure is repeated until the capillary pressures converge towards specific values such that $(P_c, i)_{new} - (P_c, i)_{old} < \epsilon$ with $\epsilon = 10^{-5}$.

As a result, a series of K-values will be generated as a function of liquid pressure and pore radius $K(P^L, r)$. The pressure range used goes from 20 bars to 200 bars, whereas the pore radius used goes from 5 nm to 100 nm with increments of 2 bars and 5 nm respectively.

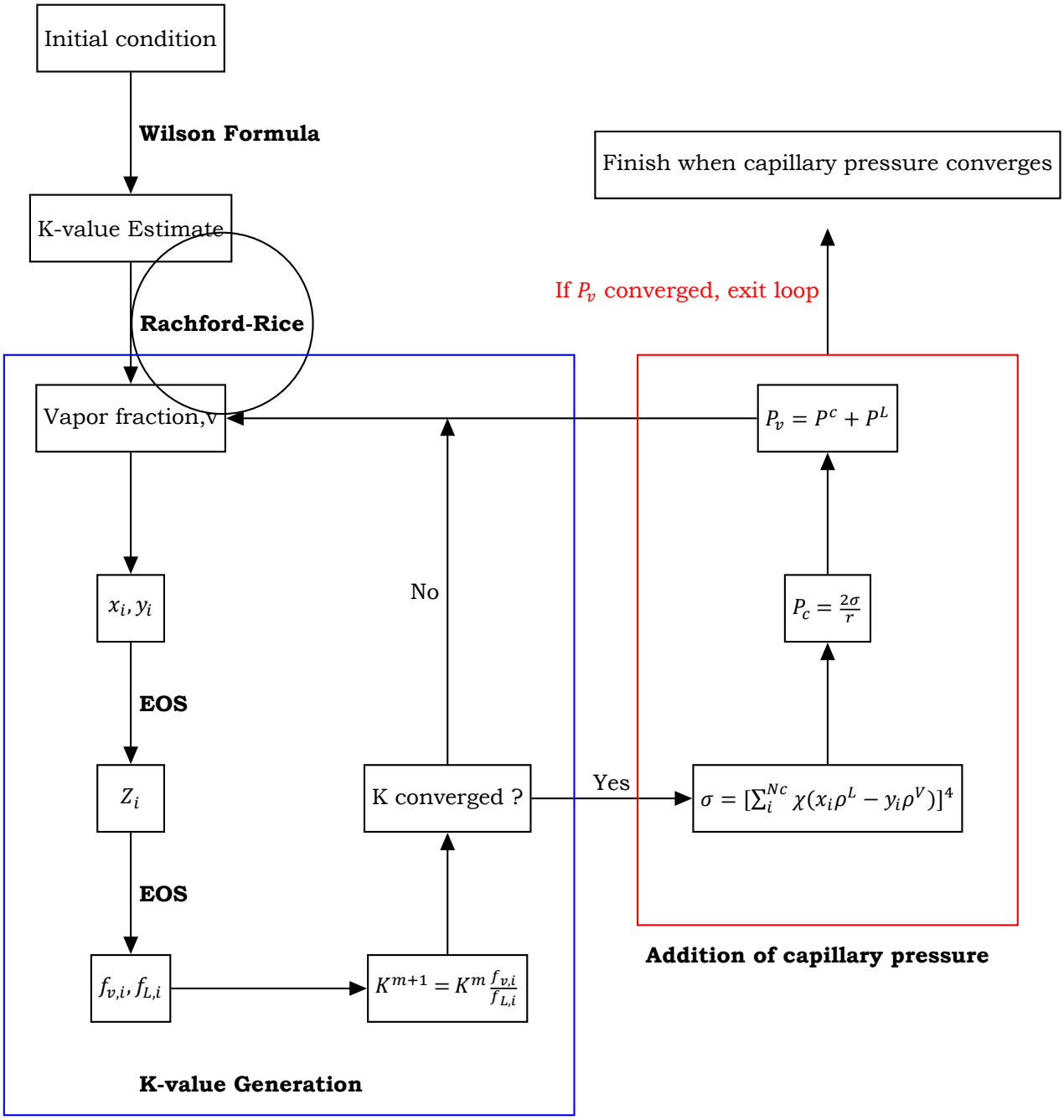
Initial condition
Wilson Formula
K-value Estimate
Rachford-Rice
Vapor fraction,v
x_i, y_i
EOS
Z_i
EOS
$f_{v,i}, f_{L,i}$
$K^{m+1} = K^m \frac{f_{v,i}}{f_{L,i}}$
K converged ?
No
Yes
$\sigma = [\sum_i^{Nc} \chi(x_i\rho^L - y_i\rho^V)]^4$
$P_c = \frac{2\sigma}{r}$
$P_v = P^c + P^L$
If P_v converged, exit loop
Finish when capillary pressure converges
K-value Generation
Addition of capillary pressure

3

Validation of modified K-value method

The modified K-value method needs to be validated first before running dynamic simulations.

A standard compositional simulator was developed in Matlab using the natural formulation [2]. We added a capillary pressure into fugacity constraint to compare results of rigorous EoS-based calculations with the modified K-value method. The following sections explain details of simulation model and modifications.

3.1. Jacobian matrix

In this section, we describe solution details of nonlinear system (2.2)-(2.8). The solution requires using Newton-Raphson method to linearize the system, in which a Jacobian matrix is created and solved for each iteration. In mathematical terms, it can be written as:

$$\mathbf{R}(\mathbf{X}) = 0 \tag{3.1}$$

Where **R** is a nonlinear operator (or residual) consisting of a set of equations and **X** is a set of variables. A Jacobian matrix is developed in order to solve the solution vector **x**:

$$\mathbf{J}\delta = -\mathbf{R} \tag{3.2}$$

Where $\delta = \mathbf{x}^{k+1} - \mathbf{x}^{k}$ and each entry J_{ij} in the Jacobian matrix **J** is the derivative of equation R_i with respect to variable x_j or $J_{ij} = \frac{\partial R_i}{\partial x_j}$.

We iterate until the residual converges towards an infinitesimal value ϵ. $\|\mathbf{R}\| < \epsilon$. Given a hydrocarbon system containing N_c components in both a liquid and gaseous states, the number of unknowns for a given cell i would be $(2N_c + 4)$: x_1, x_2,..., x_{N_c}, y_1, y_2,..., y_{N_c}, S_o, S_w, S_w, P_i.

The number of equations required to solve that would be $(2N_c + 4)$. The latter were split between primary and secondary equations as such:

Primary equations:

$$F_p^c = -\frac{V_i \partial}{\partial t}\left[\phi(\rho_o S_o x_c + \rho_g S_g y_c)\right] + \sum_j^n \left[x_c \rho_o \frac{K k_{ro}}{\mu_o}\frac{A_{ij}}{l_{ij}}(P_j - P_i) + y_c \rho_g \frac{K k_{rg}}{\mu_g}\frac{A_{ij}}{l_{ij}}(P_j - P_i)\right] \tag{3.3}$$

$$F_p^{N_c+1} = -\frac{V_i \partial}{\partial t}\left[\phi(\rho_w S_w)\right] + \sum_j^n \left[x_c \rho_o \frac{K k_{ro}}{\mu_o}\frac{A_{ij}}{l_{ij}}(P_j - P_i) + y_c \rho_g \frac{K k_{rg}}{\mu_g}\frac{A_{ij}}{l_{ij}}(P_j - P_i)\right] \tag{3.4}$$

Secondary equations:

$$F_s^1 = \sum_{j=1}^{N_c} x_c - 1, \quad F_s^2 = \sum_{j=1}^{N_c} y_c - 1 \tag{3.5}$$

$$F_s^3 = S_o + S_g + S_w - 1 \tag{3.6}$$

$$F_s^{3+c} = \psi_c^L x_c - \psi_c^V y_c \tag{3.7}$$

Similarly, the variables would be split between primary and secondary as such (for 8 components):

$\mathbf{X_p} = [y_3 \quad y_4 \quad y_5 \quad y_7 \quad y_8 \quad S_o \quad S_g \quad P]$

$\mathbf{X_s} = [x_1 \quad x_2 \quad x_3 \quad x_4 \quad x_5 \quad x_6 \quad x_7 \quad x_8 \quad y_1 \quad y_2 \quad S_w]$

The simulation starting point is declared at specific molar compositions, saturations and reservoir pressure (equivalent to the liquid pressure). At time t = 0, $\mathbf{X_p} = \mathbf{X_p^0}$ and $\mathbf{X_s} = \mathbf{X_s^0}$.

The variables at the next time step $(v+1)$ are computed by using Newton-Raphson as such:

$$\begin{bmatrix} \mathbf{X_p^{v+1}} \\ \mathbf{X_s^{v+1}} \end{bmatrix} = \begin{bmatrix} \mathbf{X_p^v} \\ \mathbf{X_s^v} \end{bmatrix} - \begin{bmatrix} \mathbf{F_p^v} \\ \mathbf{F_s^v} \end{bmatrix} / \begin{bmatrix} \frac{\partial \mathbf{F_p}}{\partial \mathbf{X_p}} & \frac{\partial \mathbf{F_p}}{\partial \mathbf{X_s}} \\ \frac{\partial \mathbf{F_s}}{\partial \mathbf{X_p}} & \frac{\partial \mathbf{F_s}}{\partial \mathbf{X_s}} \end{bmatrix}$$

The derivations of the equations $\frac{\partial \mathbf{F_p}}{\partial \mathbf{X_p}}, \frac{\partial \mathbf{F_p}}{\partial \mathbf{X_s}}, \frac{\partial \mathbf{F_s}}{\partial \mathbf{X_p}}, \frac{\partial \mathbf{F_s}}{\partial \mathbf{X_s}}$ are explained in the appendix.

3.2. Discretisation

The equations described in the previous sections are already discretized in space. Now we can discretize them in time and define time approximation scheme. An implicit approach is preferred over an explicit one since it offers a stable solution regardless of the CFL number (which is correlated to the time-step), the upper-script v represents the current time step whereas *(v+1)* is the subsequent one. A distinct mass balance equation will be attributed to every single component in the hydrocarbon as well an additional one for the water. Therefor, there will be $(N_c + 1)$ primary mass balance equations.

The primary mass balance equations for the hydrocarbon components will be discretized in the following manner:

$$F_p^{c,v+1} = -\frac{V_i}{\Delta t}\left[\phi^{v+1}(\rho_o S_o x_c + \rho_g S_g y_c)^{v+1} - \phi^{v}(\rho_o S_o x_c + \rho_g S_g y_c)^{v}\right] + \sum_j^n \left[x_c \rho_o \frac{Kk_{ro}}{\mu_o}\frac{A_{ij}}{l_{ij}}(P_j - P_i) + y_c \rho_g \frac{Kk_{rg}}{\mu_g}\frac{A_{ij}}{l_{ij}}(P_j - P_i)\right]^{v+1}, \quad c = 1, 2, ..., N_c \tag{3.8}$$

For the water phase, the associated primary equation would be:

$$F_p^{N_c+1,v+1} = -\frac{V_i}{\Delta t}\left[\phi^{v+1}(\rho_w S_w)^{v+1} - \phi^{v}(\rho_w S_w)^{v}\right] + \sum_j^n \left[x_c \rho_o \frac{Kk_{ro}}{\mu_o}\frac{A_{ij}}{l_{ij}}(P_j - P_i) + y_c \rho_g \frac{Kk_{rg}}{\mu_g}\frac{A_{ij}}{l_{ij}}(P_j - P_i)\right]^{v+1} \tag{3.9}$$

Moreover, the $(N_c + 3)$ secondary equations would be:

$$F_s^{1,v+1} = \sum_{j=1}^{N_c} x_c^{v+1} - 1, \quad F_s^{2,v+1} = \sum_{j=1}^{N_c} y_c^{v+1} - 1 \tag{3.10}$$

$$F_s^{3,v+1} = S_o^{v+1} + S_g^{v+1} + S_w^{v+1} - 1 \tag{3.11}$$

$$F_s^{c+3,v+1} = \left(\psi_c^L x_c - \psi_c^V y_c\right)^{v+1}, \quad c = 1, 2, ..., N_c \tag{3.12}$$

3.3. Compositional simulator with added capillary pressure

The addition of capillary pressure will result in a shift between the vapor pressure and the liquid pressure for each component. Each cell will therefor contain 2 separate pressures. Adding capillary pressure to the mass balance equation results in the following modification:

$$\frac{V_i \partial}{\partial t}\left[\phi(\rho_o S_o x_c + \rho_g S_g y_c)\right] = \sum_j^n \left[x_c \rho_o \frac{Kk_{ro}}{\mu_o}\frac{A_{ij}}{l_{ij}}(P_j - P_i) + y_c \rho_g \frac{Kk_{rg}}{\mu_g}\frac{A_{ij}}{l_{ij}}[(P + P_{cap})_j - (P + P_{cap})_i]\right] \tag{3.13}$$

The capillary pressure would be calculated as a function of liquid pressure, temperature and molar composition using a combination of Peng-Robinson EOS, Laplace and Parachor similar to the method described in 2.3.2 and 2.3.3.

Moreover, capillarity effects will also be incorporated in the fugacity coefficients for every single component.

$$\psi_c^{L*} x_c - \psi_c^{V*} y_c = 0, \quad c = 1, 2, ..., N_c \tag{3.14}$$

Where ψ^{L*} and ψ^{V*} are modified fugacity coefficients, such that $\psi^{V*} = \frac{f_i^V}{y_i P^V}$ and $\psi^L = \frac{f_i^L}{x_i P^L}$. The fugacity coefficients are computed via:

$$ln(\frac{f_i^P}{y_i P^P}) = \frac{b_i}{b^P}(Z^P - 1) - ln(Z^P - B) - \frac{A}{2B\sqrt{2}}(\frac{2\sum_j y_j a_{ji}}{a^P} - \frac{b_i}{b^P})ln(\frac{Z^P + (\sqrt{2}+1)B}{Z^V - (\sqrt{2}-1)B}) \quad (3.15)$$

The above equation is described in section 2.3.3. (the upper script P designates the phase of the component).

3.4. Comparison results

The results for both modified K-value method described in chapter 2 and the modified compositional simulator (with fugacity constraint) described in this chapter are shown in Figures 3.1 and 3.2. A well with a homogeneous pore radius of 10 nm is depleted for three days from a starting pressure of 120 bars and the pressure profiles for both methods are drawn.

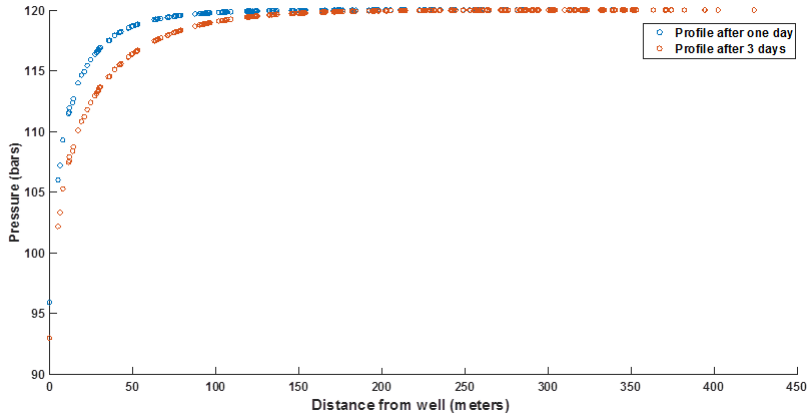

Figure 3.1: Pressure Profiles after one and 3 days for modified K-value method

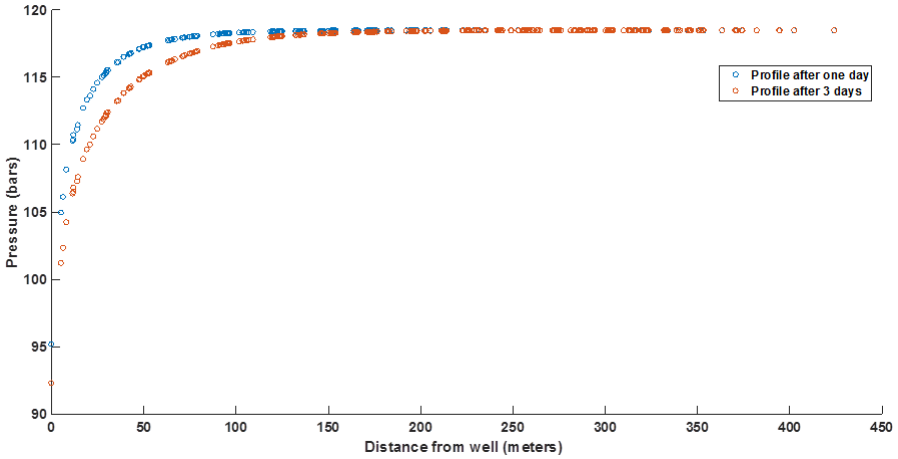

Figure 3.2: Pressure Profiles after one and 3 days for modified compositional method with fugacity constraint

Comparing both methods reveals very similar results. Both 3-days pressure profiles are compared and the differences between are as low as 1%.

Another way to confirm the modified K-value method is to compare results between that

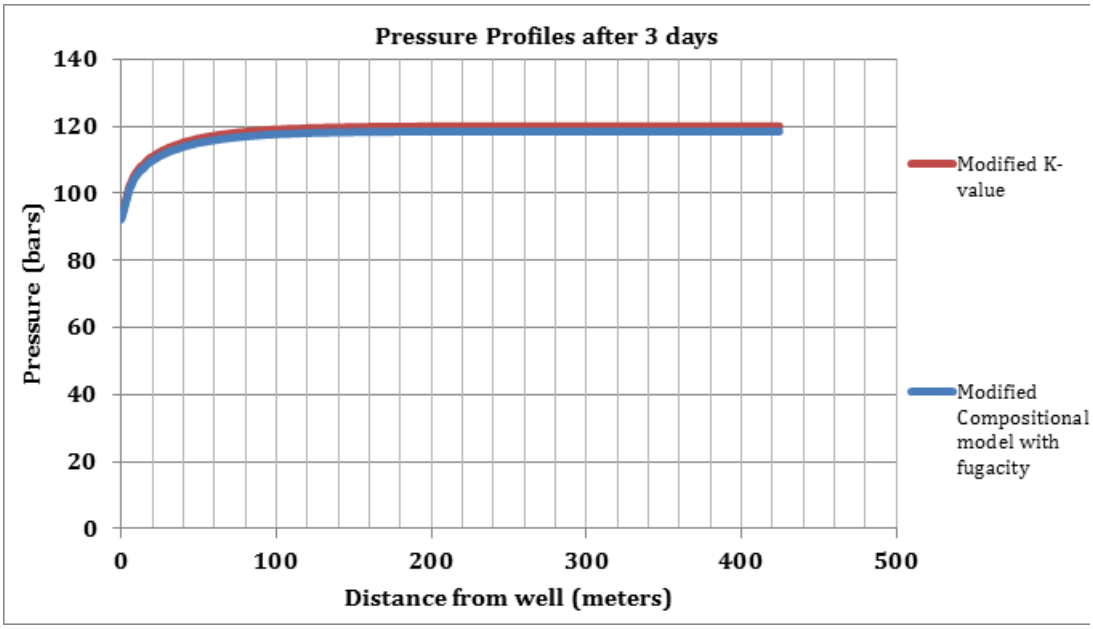

Figure 3.3: Comparison between modified K-value method and modified compositional method using fugacity constraint

method in a high porosity medium and a standard compositional simulator without any modifications. For K-values extracted for larger porosity (and subsequently larger pore radius), the capillary pressure should be insignificant and consequently the pressure and saturation results should match that of a standard compositional simulator in similar conditions.

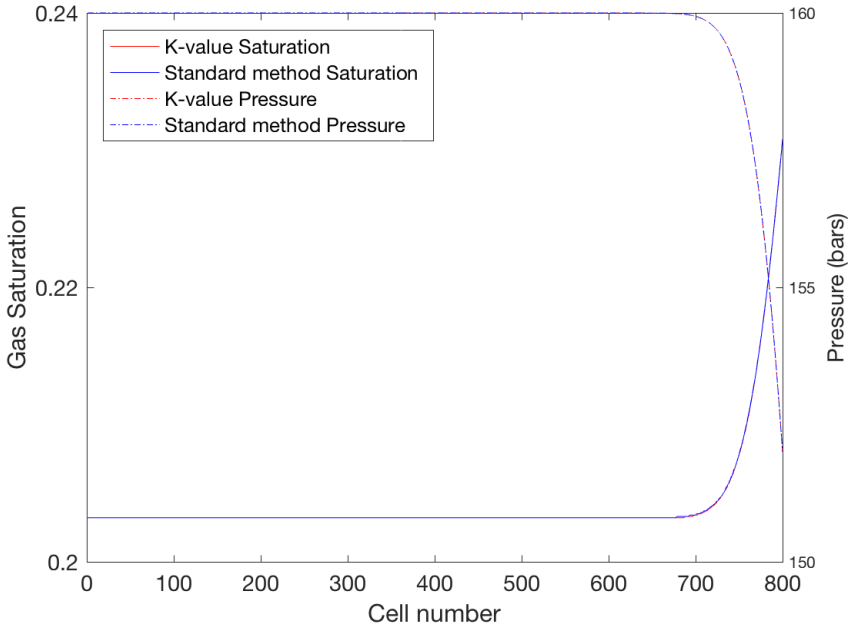

Figure 3.4: Comparison between modified K-value method and standard compositional method for a high porosity medium

Fig. 3.4 shows the gas saturation and pressure profiles from a reservoir comprised of 800 cells after 50 days of depletion starting from a pressure of 160 bars (the well is located at cell 800). Both sets of values from both methods are nearly identical. This helps prove that the modified K-value method can be used for further case studies.

4

Simulation results

4.1. Inputs

Bakken oil sample was used as input for the generation of the modified K-values, similar to the one used by Nojabaei [15]. The molar composition and chemical properties of that sample are shown in the table below.

Component	Molar fraction	Molar weight	P_c (psi)	T_c (F)	ω	Parachor Coefficient
C_1	0.36736	16.535	655.02	335.336	0.0102	74.8
C_2	0.14885	30.433	721.99	549.969	0.1028	107.7
C_3	0.09334	44.097	615.76	665.97	0.152	151.9
C_4	0.05751	58.124	546.46	759.208	0.1894	189.6
$C_5 - C_6$	0.06406	78.295	461.29	875.479	0.2684	250.2
$C_7 - C_{12}$	0.15854	120.562	363.34	1053.25	0.4291	350.2
$C_{13} - C_{21}$	0.0733	220.716	249.61	1332.095	0.7203	590
C_{22+}	0.03704	443.518	190.12	1844.491	1.0159	1216.8

4.2. Modified K-values

The modified K values were generated for several pore radii and pressure values for each individual component. The pressure range was set between 20 and 200 bars with increments of 2 bars; whilst, it was set between 5 and 200 nm with increments of 5 nm for radius values.

An example of modified K-values is shown in Fig. 4.1. At 20 bars, the modified K-values increase logarithmically with the pore radius, converging towards the standard K-value undisturbed by capillarity effects. The largest effects occur between 0 and 100 nm. Above the latter value, the differences become less significant.

The K-value is defined as the ratio of the vapor phase of a component to its liquid phase. Therefor, at lower pore radius values where the K-value is significantly lower, the liquid phase of the component C_1 will be more prevalent than in a medium with a higher pore radius.

Another note is the effect of liquid pressure on the K-values as seen in Fig. 4.2. The most

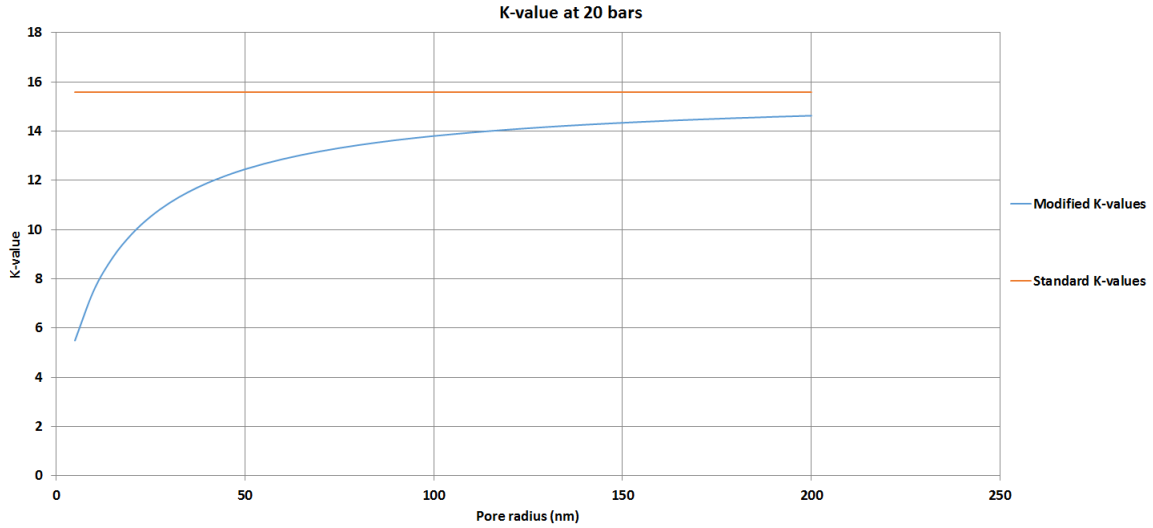

Figure 4.1: K Values generated at 20 bars for C1 component

notable shifts occur at lower pressures. At P=20 bars, the modified K-value changes from 5.49 to 14.62 where the radius shifts from 5 to 200 nm (a 166.4 % increase), whereas the shift seen at 190 bars is from 1.78 to 1.83 (2 % increase). Hence, we can determine that the effects of confinement become more severe for lighter components the longer the well is depleted.

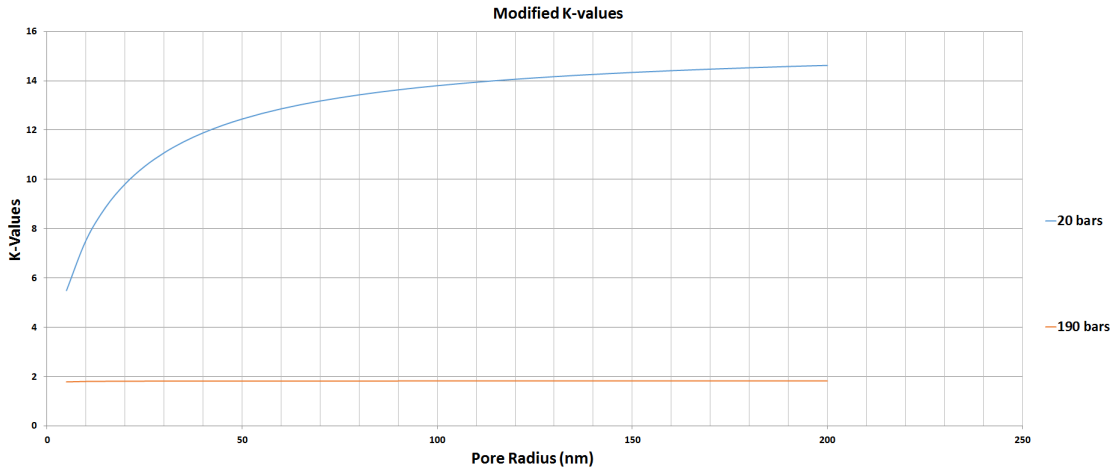

Figure 4.2: Effects of pressure on K-values for component C1

The effects of liquid pressure and pore radius can be noted more visibly in Fig.4.3. Above 150 bars, all three curves on the plot seem to merge indicating that capillary pressure effects become nearly insignificant at that said pressure. Moreover, the K-value shift from 100 nm to 5 nm at 20 bars is substantial, confirming that the most notable confinement effects occur below 100 nm.

4.3. Bubble Point reduction

The Bubble point (BBP) was calculated for both confined and non-confined spaces at several pressure and temperatures. For a given molar composition, the BBP can be determined via trial and error using a combination of flash calculation and Peng-Robinson EOS to deter-

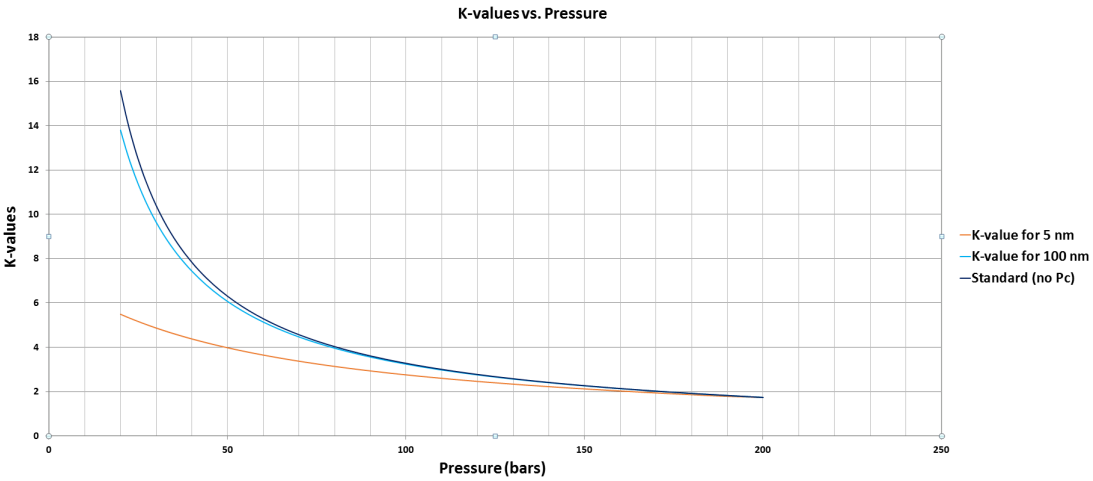

Figure 4.3: Effects of pressure and radius on K-values for component C1

mine the specific K-values for each component. For confined spaces that take into account capillary pressure, the Parachor and Laplace equations are added to the aforementioned combination to calculate the modified K-value (refer to Chapter 2). In the end, the equality $\sum K_i z_i = 1$ needs to be satisfied.

Starting at a initial liquid pressure, the K-values are calculated for the Bakken sample. If $\sum K_i z_i < 1$, then the mixture is in a two-phase state and the assumed pressure is below BBP. The starting pressure is then continuously increased with smaller and smaller increments till the vapor pressure is reached. Vice versa, if $\sum K_i z_i > 1$, then the pressure is continuously decreased till the BBP is attained. Two bubble point pressures were calculated: one for tight confined spaces and one for regular spaces.

The results can be seen in Fig.4.4. Confirming the results observed in the previous section, the largest bubble point reduction occurs at lower pressures and temperatures.

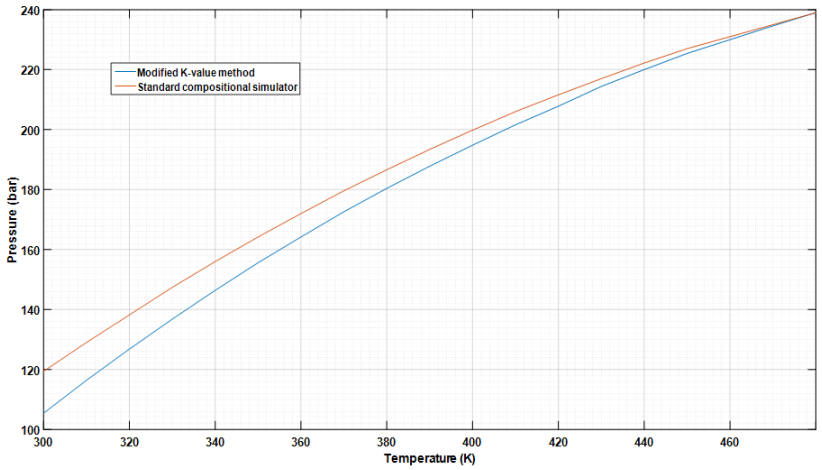

Figure 4.4: Bubble Point Reduction in confined medium with 10 nm pore radius

4.4. One-dimensional models

The following comparisons were made for 1D models:

1. Standard compositional method vs. modified K-value method in a one-dimensional homogeneous medium at starting pressures above the bubble point pressure. In this scenario, the hydrocarbon mixture is in a pure liquid state initially. The objective of this comparison is to reveal the late gas generation in a confined space as well as to study the difference in production profiles between both methods.
2. Standard compositional method vs. modified K-value method in a homogeneous medium with a vertical feature similar to a fracture. The objective of these comparisons is to study the behavior of the gas formed within the feature and its propagation within the rest of the matrix.

4.4.1. Homogeneous media

Model description

The first comparison was made between a standard compositional approach and the modified K-value method. For that, two mediums were generated with porosity of 20% and 2%; the associated pore radii are 58.833 nm and 1.804 nm respectively. In total, four simulations were performed in a simple one-dimensional setup with following parameters:

- Total length of 40 meters, with 80 cells in the x-direction (d_x = 0.5 m);
- production well is located at the right as shown in Fig. 4.5;
- uniform homogeneous permeability (100 mD in all simulations) and corresponding porosity;
- well is controlled at a constant oil production rate of 2 m^3/day.

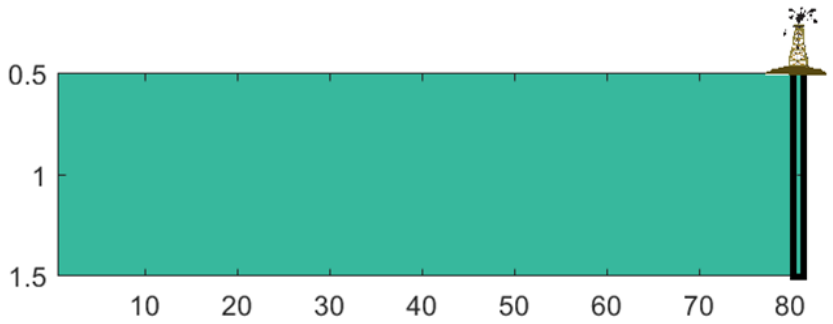

Figure 4.5: Comparison of GPR for Standard method and Modified K-value method

In the first comparison, we study the effect of capillary pressure, correlated to the pore radius, to overall production. All the simulations were started from an elevated pressure (200 bars) where mixture is at liquid phase.

Results in a low porosity medium

Fig.4.7 shows the saturation and pressure profiles for both methods in a confined medium (2 % porosity). Initially, the entire block is in the liquid phase. Once, the pressure starts getting depleted, the vapor phase starts appearing earlier in the confined cells; the K-value-based gas saturation curve (dark blue) lags behind the gas saturation curve for the standard model. Moreover, the pressure drop in the K-value method is sharper than in the conventional EoS-based method at times t = 0.0001 days and t = 0.0003 days; this is explained by the fact

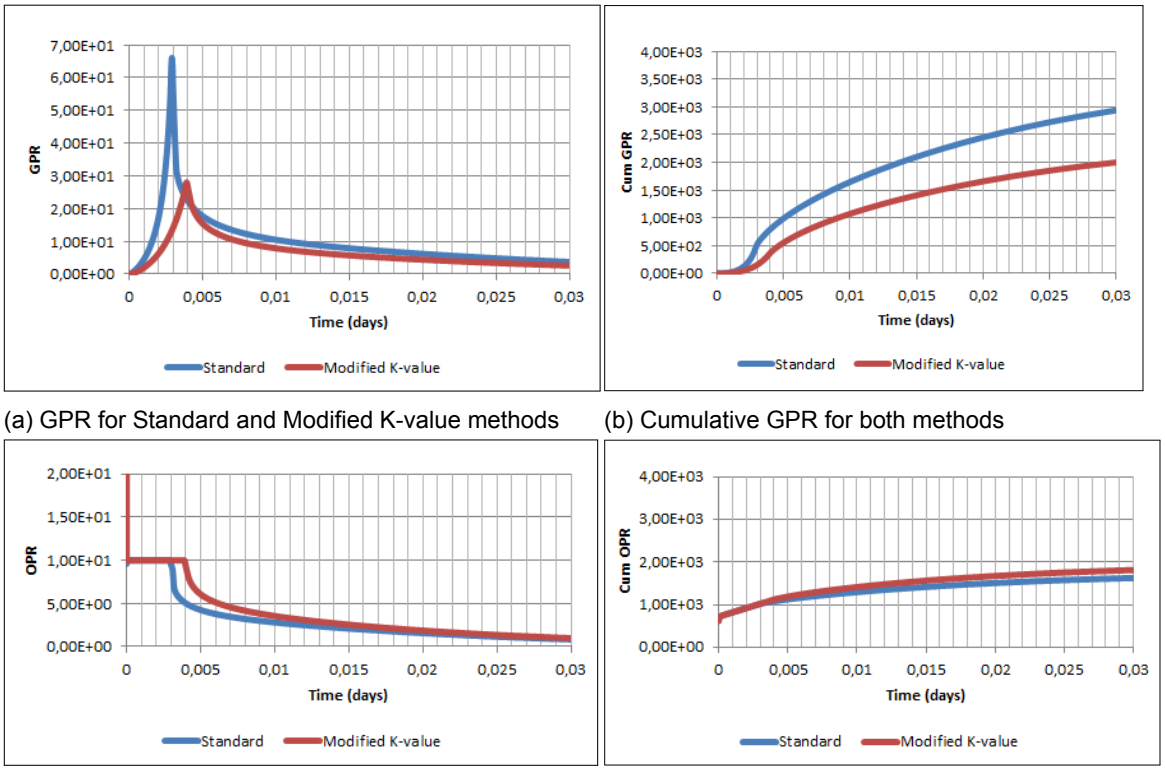

(a) GPR for Standard and Modified K-value methods

(b) Cumulative GPR for both methods

(c) OPR for Standard and Modified K-value methods

(d) Cumulative OPR for both methods

Figure 4.6: Production Profiles in 2% porosity medium

that less gas is generated in the K-value method which reduces the mobility of the phase and requires a larger pressure gradient.

After 0.05 days, there is a noticeable change in oil and gas productions between both methods. Due to the reduction in bubble point pressure, gas phase starts to appear earlier in most cells in the modified K-value method. A 31.69% decrease in gas produced is seen whereas a 11.8% increase in oil is noted for the modified K-value simulator.

	Standard simulator	Mod. K-Value
Cum. GPR	3377.4	2307.13
Cum. OPR	2307.1	1923.51

Table 4.1: Differences in cumulative oil and gas productions in matrix of porosity

Results in a high porosity medium

The same simulation was ran in a medium with higher porosity (20%) where the capillary effects are less significant. The production profiles are seen in Fig.4.8. Both the gas production and oil production rates are nearly overlapping with the ones generated from the standard simulator. The subtle differences indicate minor capillary effects.

4.4.2. Tight media with micro-feature

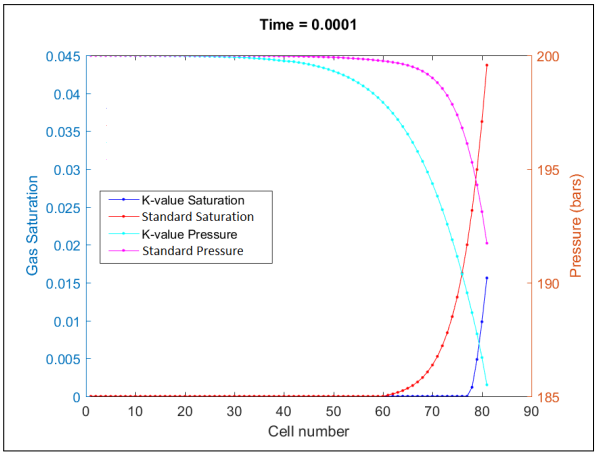

(a) At time t=0.0001 days

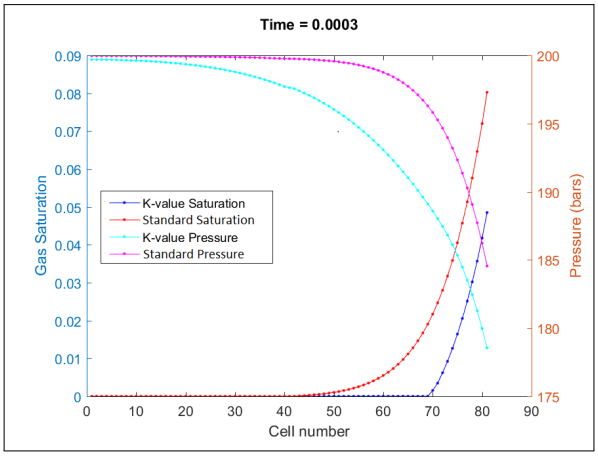

(b) At time t=0.0003 days

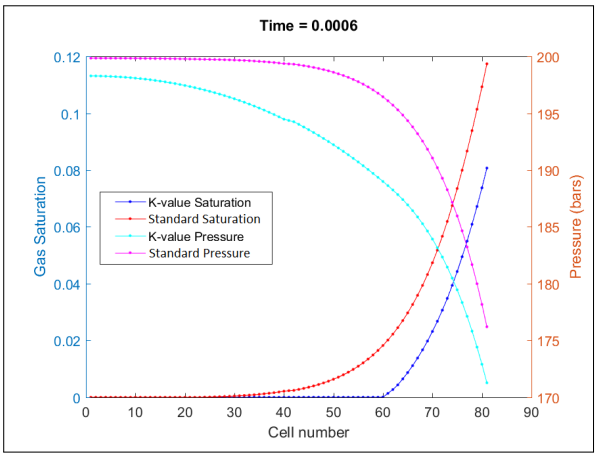

(c) At time t=0.0006 days

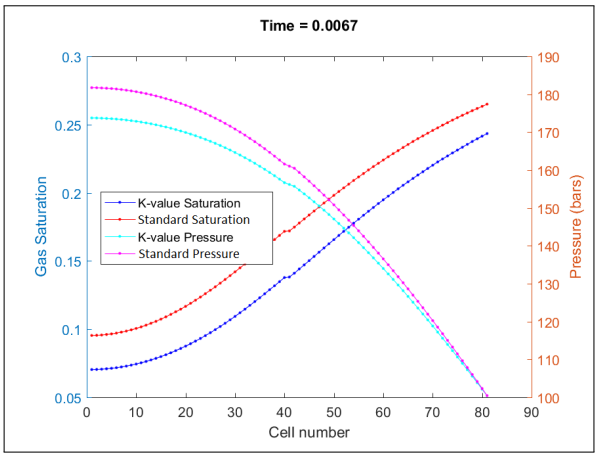

(d) At time t=0.0067 days

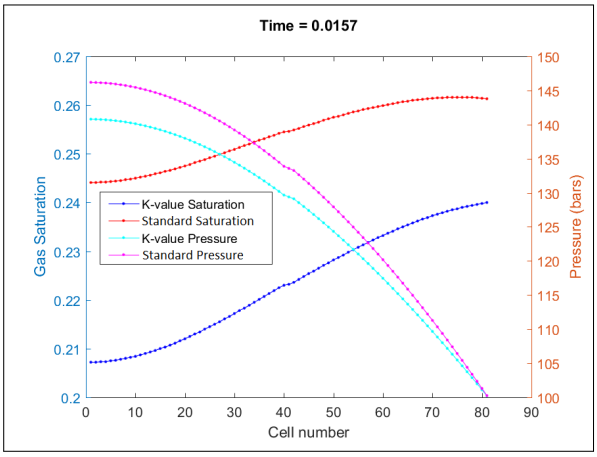

(e) At time t=0.0157 days

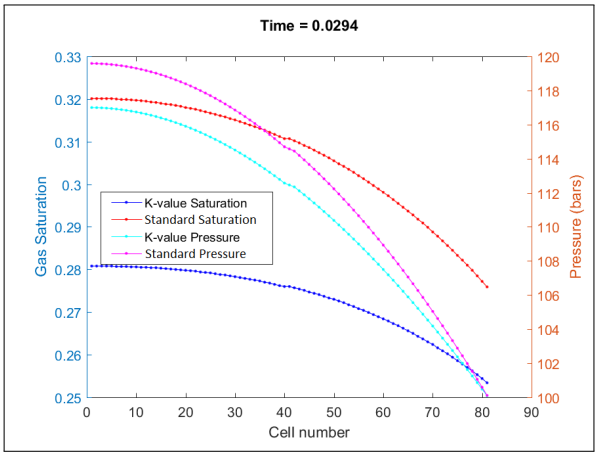

(f) At time t=0.0294 days

Figure 4.7: Saturation and pressure profiles for standard and modified K-value methods in confined matrix (2% porosity) over time

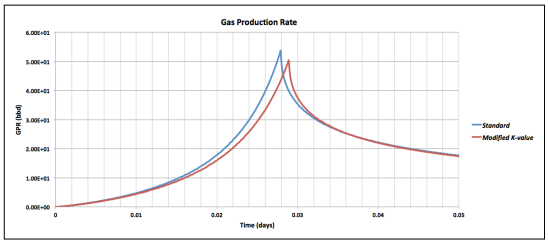

(a) GPR for Standard and Modified K-value methods

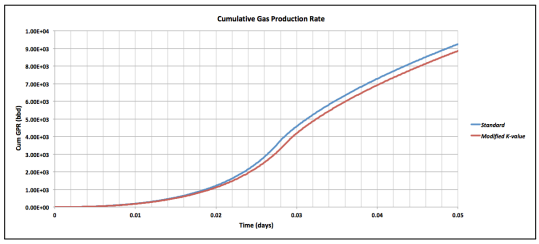

(b) Cumulative GPR for both methods

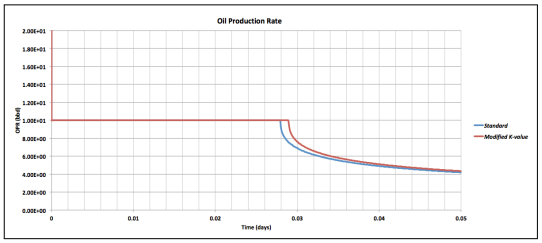

(c) OPR for Standard and Modified K-value methods

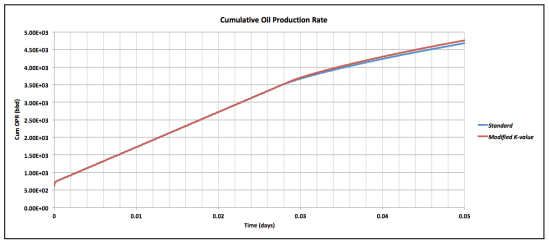

(d) Cumulative OPR for both methods

Figure 4.8: Production Profiles in 20% porosity medium

Model description

In this model we analyze the effect of a micro-feature in a tight formation. A one-dimensional tight media with a vertical micro-feature (Fig. 4.9) was introduced with the following parameters:

- Total length of 40 meters, with 800 cells in x-direction (d_x = 0.05 m).
- a one-cm feature, comprised of 10 cells, is located in the middle of the matrix (d_x = 0.001 m);
- producer well is located at the right of the reservoir;
- the matrix has the same properties as the confined shale formation (porosity of 1% and a permeability of 0.001 mDarcy), where feature has a higher porosity and permeability (20 % and 10 mDarcy);
- well is controlled at a constant oil production rate of 2 m^3/day.

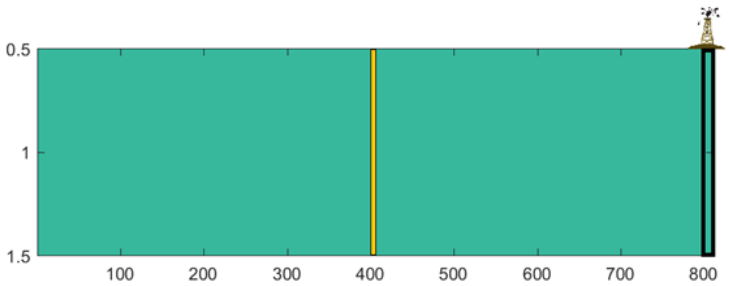

Figure 4.9: One-dimensional tight media model with micro-feature

The simulations were ran for pressures below BBP in this case. The objective is to study the behavior of gas already present in the feature and its propagation within the shale matrix. Two simulations were ran with different starting pressures of 160 and 100 bars.

Standard compositional model

The results of reservoir depletion using a standard compositional simulator with no confinement effects are shown in Fig. 4.10 and Fig. 4.11. Both pressure and gas saturation profiles were studied here. The latter don't reveal any discontinuity at the micro-feature. The gas saturation increases sharply at the well location initially, then gradually evens out throughout all the cells in the medium regardless of the porosity or permeability.

The fluid flow is uniform in a standard compositional model. No discontinuity is noted between the nano- and micro-pores.

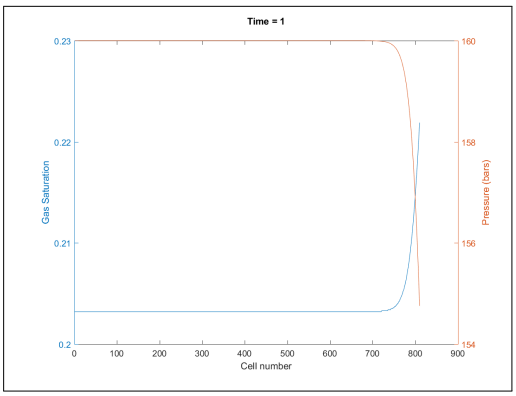

(a) At time t= 1 day

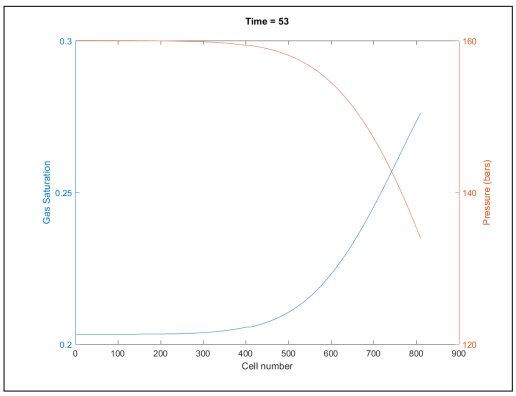

(b) At time t= 53 days

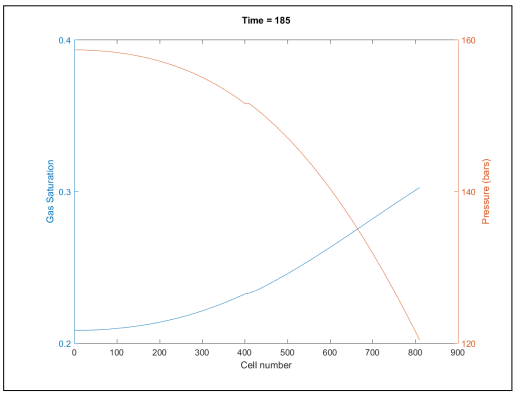

(c) At time t= 185 days

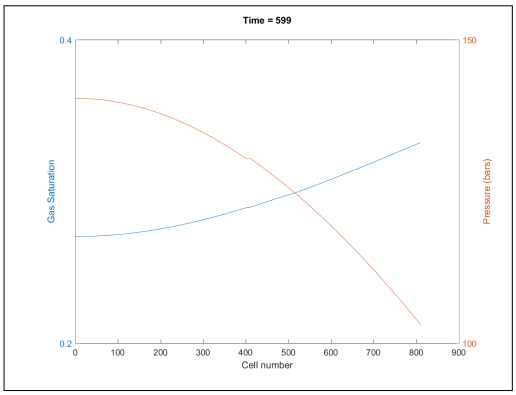

(d) At time t= 599 days

Figure 4.10: Saturation and pressure profiles in standard compositional model for the confined media with micro-feature with initial pressure at 160 bars

Results for modified K-value model

The results for the depletion process in tight reservoir with micro-feature using a modified K-value approach are shown in Fig. 4.12 with initial reservoir pressure set at 160 bars and in Fig. 4.13 with initial reservoir pressure set at 100 bars). In both cases, there is a clear discontinuity between the vertical feature and the confined media. Starting from a pressure of 160 bars in Fig. 4.12, the gas saturation in the confined matrix is 0.13 whereas it is 0.19 in the micro-feature. This is a clear effect of the bubble point reduction in smaller pores. The gas accumulated in the feature starts to shift away towards the production well at 144 days. Later, that pocket of gas draws closer to the well; the slow shift is due to the very low permeability in the shale matrix. Finally, the decrease of the gas saturation in the feature becomes more pronounced at t = 403 days and t = 583 days. Due to the reduction of the BBP, the two-phase envelop in the confined space is smaller than the standard envelop. As the pressure in the reservoir is depleted, the liquid fraction in the micro-feature decreases

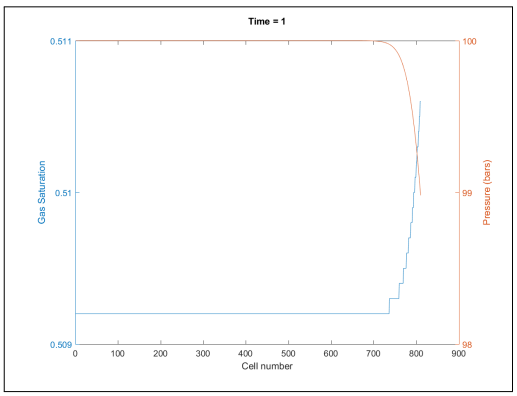

(a) At time t= 1 day

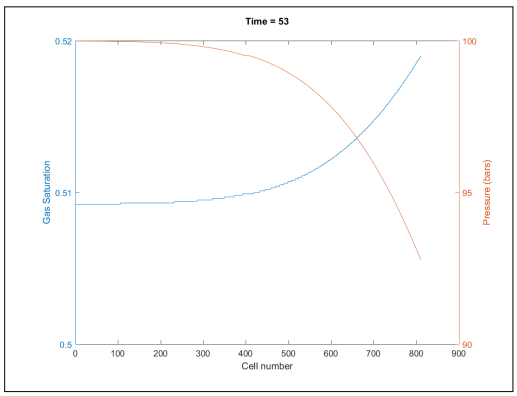

(b) At time t= 53 days

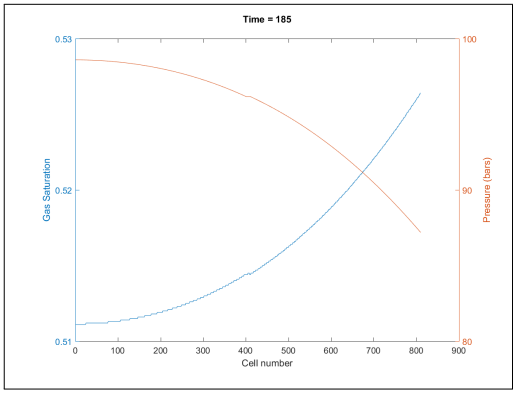

(c) At time t= 185 days

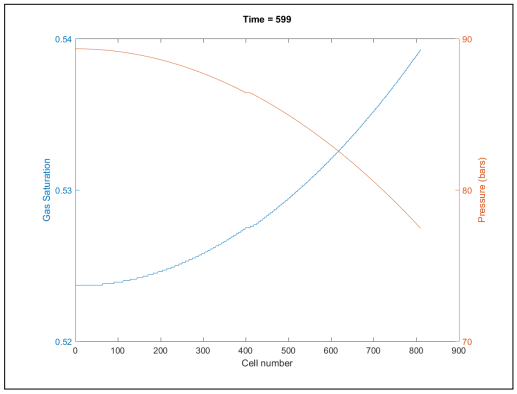

(d) At time t= 599 days

Figure 4.11: Saturation and pressure profiles in standard compositional model for the confined media with micro-feature with initial pressure at 100 bars

more slowly than in the shale matrix.

This effect can be seen even more clearly in Fig. 4.13.There is a sharp drop in gas saturation in the feature relatively to the rest of the confined media.

4.5. Two-dimensional model for fractured shale reservoir

A Discrete Fracture and Matrix (DFM) model was designed using unstructured griding in GMesh [7]. Unstructured grids were discretized with a finite volume method. The grid was separated into two physical entities: the shale matrix cells and fracture cells. A specific set of properties was attributed for each entity as described in Table 4.2.

	Porosity	Permeability	kv/kh
Shale cells	0.01	0.001	0.2
Fracture cells	1	100	1

Table 4.2: GMesh Properties

Two models were created: one realization with a coarser mesh contained 928 control volumes (Fig. 4.14) and another realization with more refined mesh contained 5654 control volumes (Fig. 4.15). The first model contains a well-connected fracture system, whereas the second shows independent systems of fractures within the shale matrix. Both models are squared-shaped with side lengths of 110 meters and a producer well perforated to the fracture (see yellow circle for the well location).

It is a well known fact that the liquid mobility in tight media is limited. To address this feature, two sets of comparisons were made: ① Standard compositional model vs. and Modified K-value method ② with normal liquid mobility (same in nano- and micro-porosity) and limited liquid mobility (no liquid flow in nano-porosity).

- Standard compositional
- Modified K-value method
- Standard compositional with limited oil mobility in tight media
- Modified K-value method with limited oil mobility in tight media

Realization 1: coarser mesh

The cumulative gas and oil production rates at 1000 days are plotted in Fig. 4.16 and Fig. 4.17. The standard method overestimates the gas saturation initially leading to a shift in the cumulative gas saturation seen in the early stages of depletion compared to the modified K-value method. This holds independent of liquid mobility in tight matrix.

The limitation in liquid mobility has similar effects on both the K-value method and the standard method. The oil is produced almost entirely in the initial stages of depletion, it can be assumed that it originates from the fractures given that the liquid phase in the shale is immobile. Moreover, the limited oil mobility increases the cumulative gas production rate. This could be explained by the fact that the liquid fractional flow is decreased, which causes an increase in the gas fractional flow and leads to a surge of gas.

The cumulative production results for the coarser grid can be seen in table4.3:

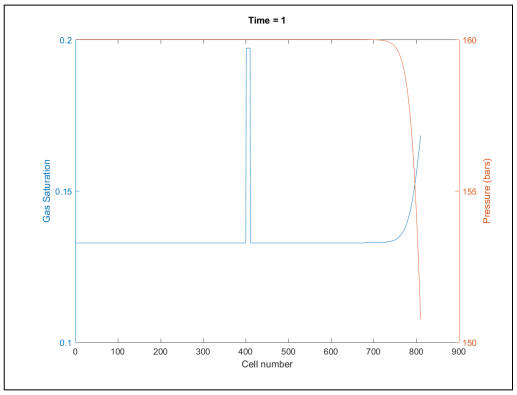

(a) At time t= 1 day

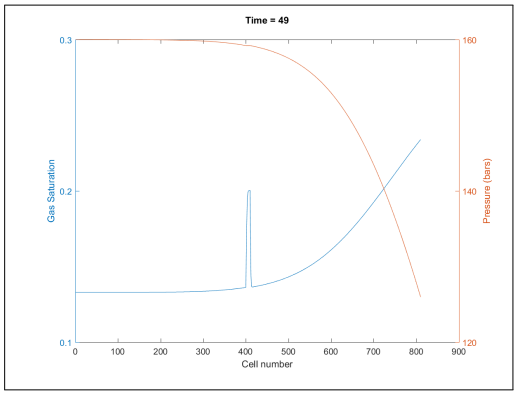

(b) At time t= 49 days

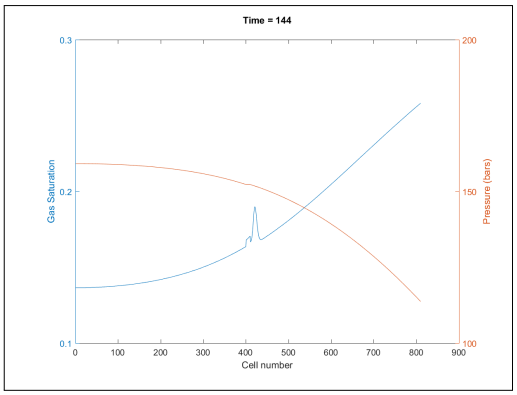

(c) At time t= 144 days

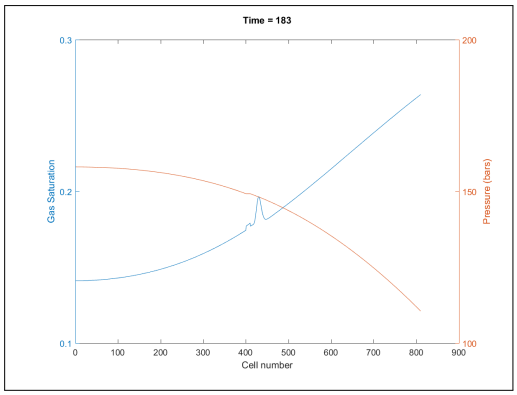

(d) At time t= 184 days

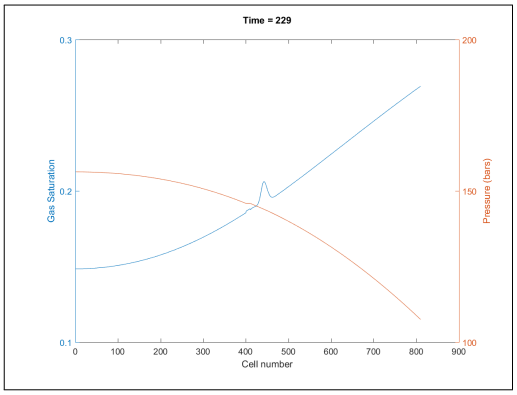

(e) At time t= 229 days

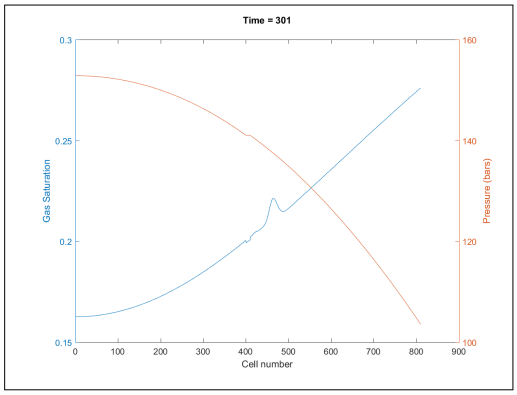

(f) At time t= 301 days

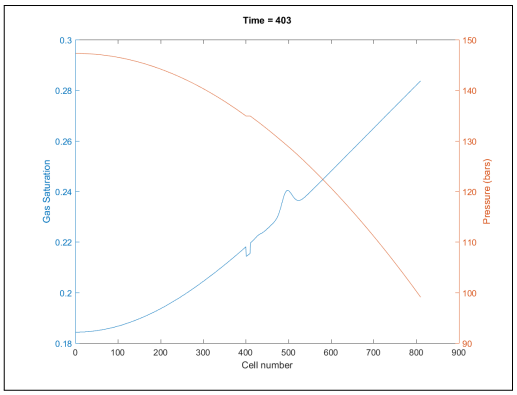

(g) At time t= 403 days

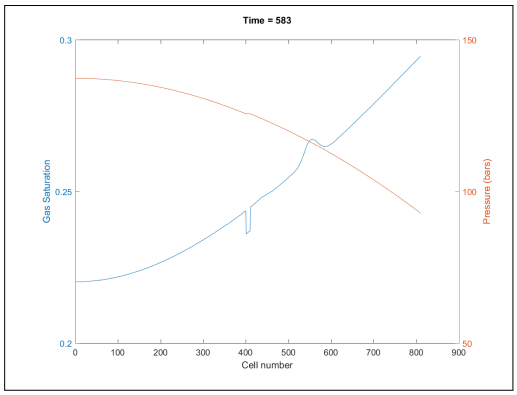

(h) At time t= 583 days

Figure 4.12: Saturation and pressure profiles for modified K-value method in confined matrix with feature over time (starting pressure 160 bars)

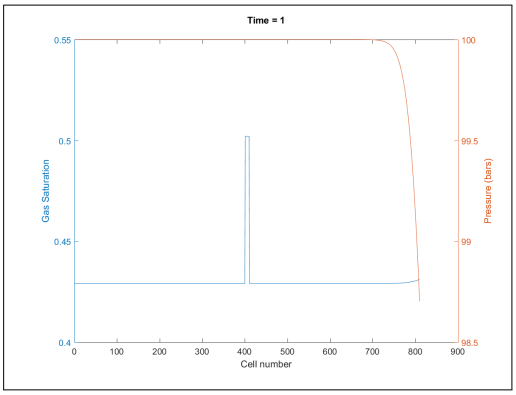

(a) At time t= 1 day

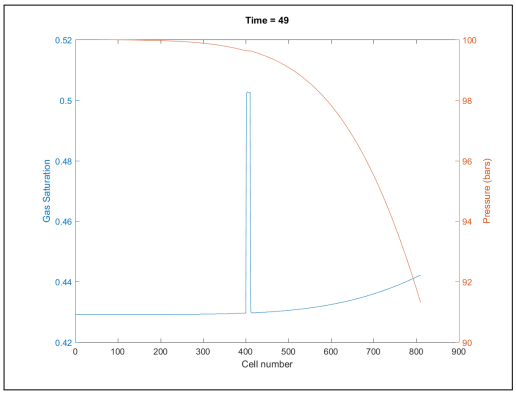

(b) At time t= 49 days

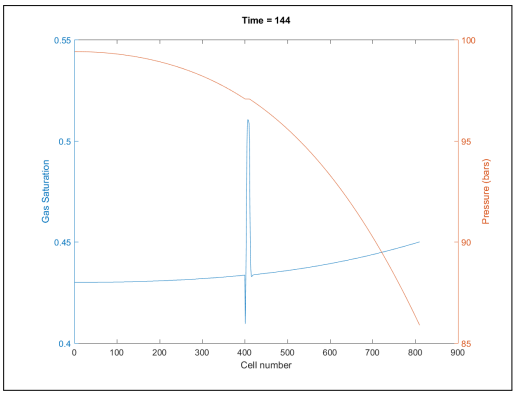

(c) At time t= 144 days

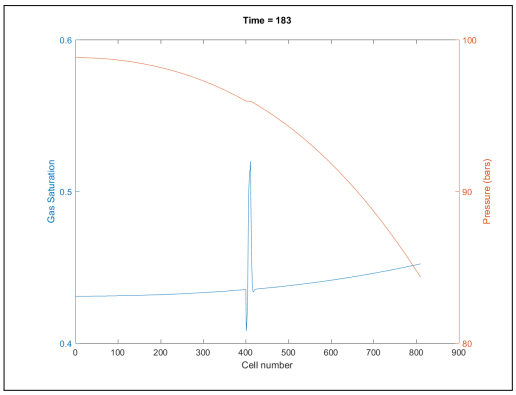

(d) At time t= 184 days

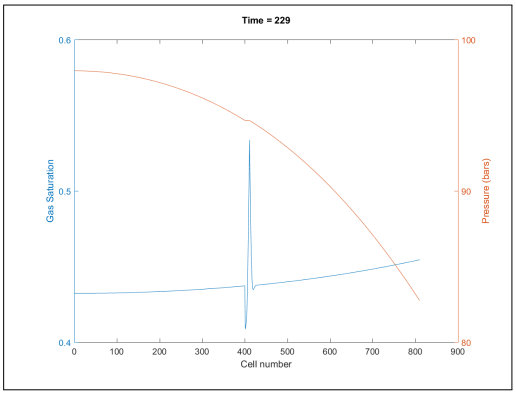

(e) At time t= 229 days

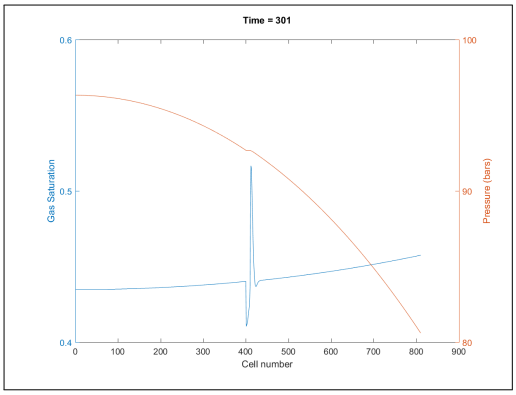

(f) At time t= 301 days

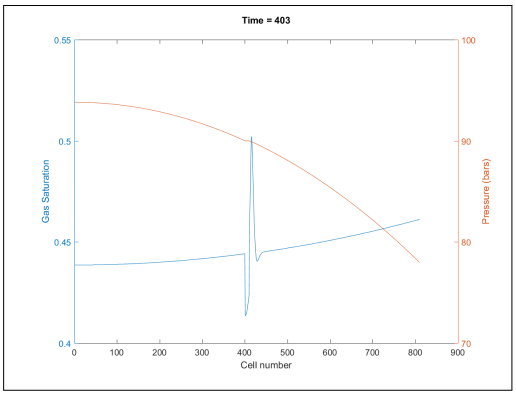

(g) At time t= 403 days

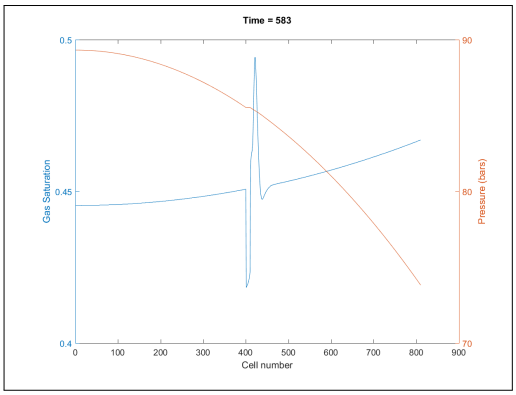

(h) At time t= 583 days

Figure 4.13: Saturation and pressure profiles for modified K-value method in confined matrix with feature over time (starting pressure 100 bars)

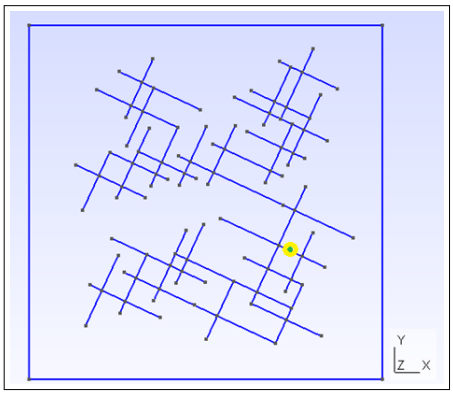

(a) Fractures inside the grid

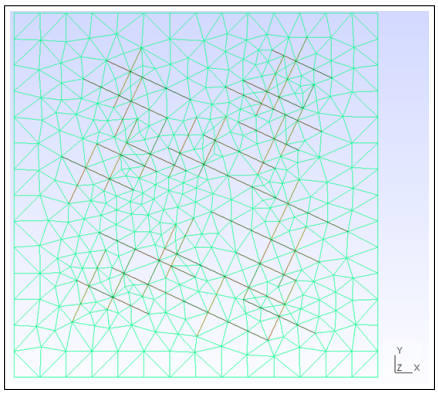

(b) Grid with Meshes

Figure 4.14: First case scenario (coarse grid)

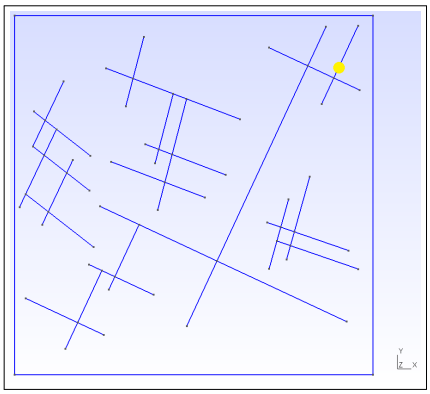

(a) Fractures inside the grid

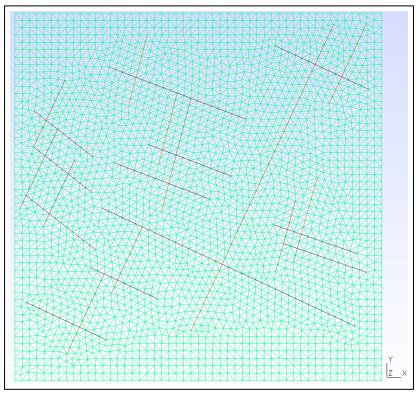

(b) Grid with Meshes

Figure 4.15: Second case scenario (finer grid)

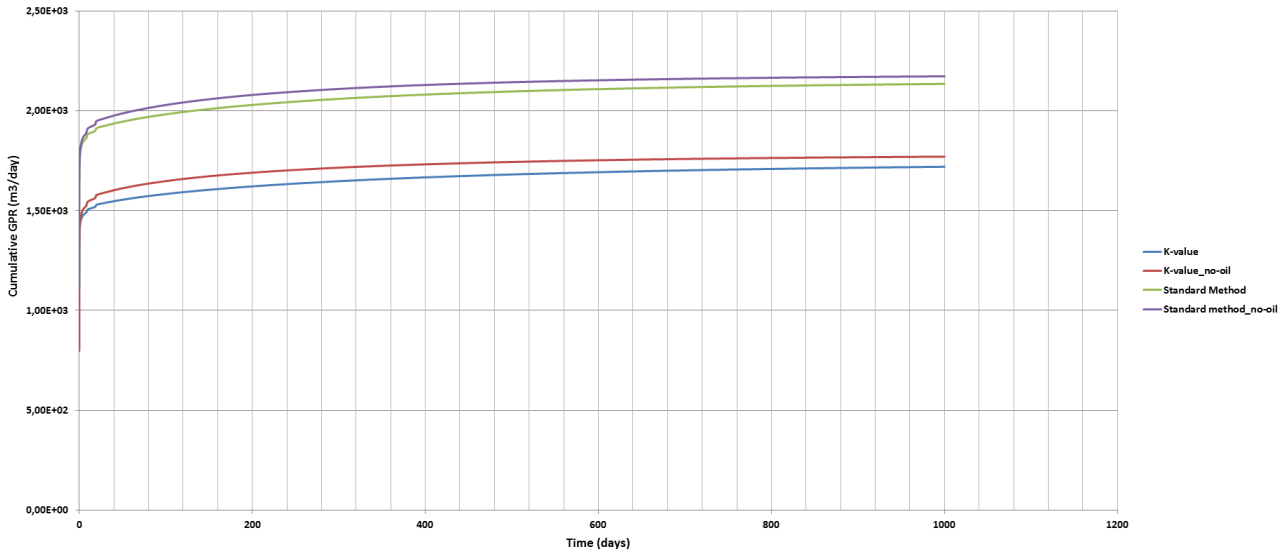

Figure 4.16: Cumulative GPR for pressure starting at 160 bars

Method used	Cum. GPR (m3/day)	Cum OPR (m3/day)
K-value	1720.24	71.01
K-value (no oil mob.)	1770.92	67.54
Standard method	2135.34	39.79
Standard method (no oil mob.)	2173.34	38.15

Table 4.3: Cumulative production results for all methods in coarse grid after 1000 days

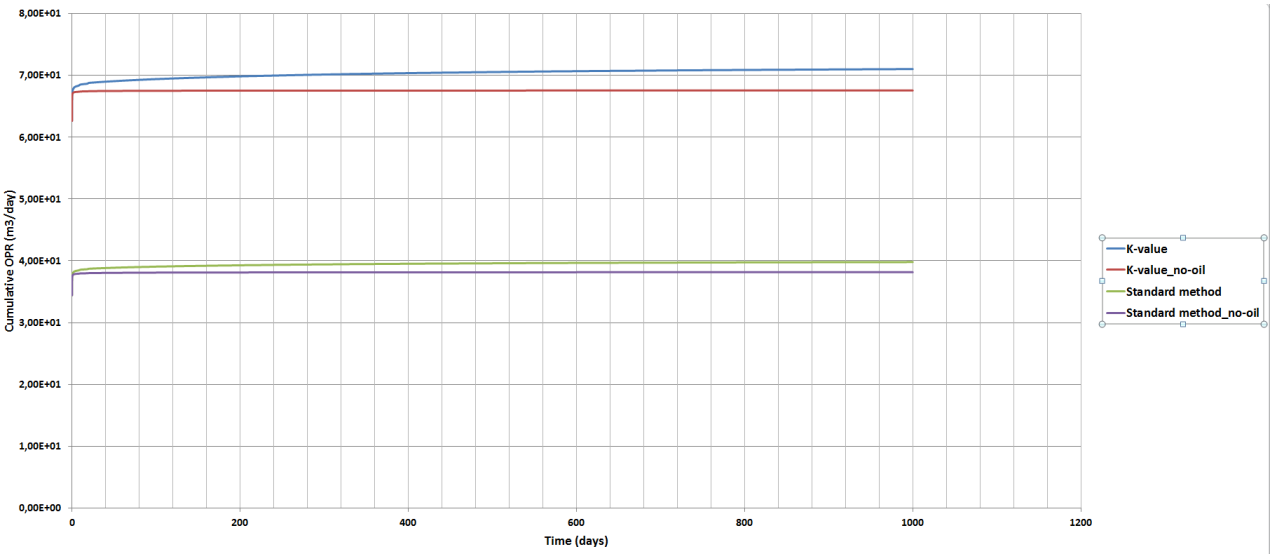

Figure 4.17: Cumulative OPR for pressure starting at 160 bars

The saturation profiles for all methods can be seen in Fig. 4.21 and Fig. 4.19. Comparing the modified K-value method and the standard compositional method regardless of oil mobility reveals that the standard simulator always overestimates the initial gas saturation, which explains the larger gas production. The gas saturation calculated in standard simulators (both with and without oil mobility) is 0.51 whereas it is 0.43 for modified K-value method for an initial reservoir pressure of 100 bars. The depletion patterns are similar for both methods, as the fracture network acts as the main pathway for the fluid to flow. The surrounding shale matrix remains unchanged for the first 200 days, the gas saturation varies slightly in the confined cells.

The pressure profiles can be seen in Fig.4.20 and Fig.4.18. The pressure profile follows the same pattern for both K-value method and standard method, as the main pressure drawdown occurs in the fracture network surrounding the producer well for the first 200 days. As the pressure differential between shale matrix and fracture cells becomes elevated enough, then the gas starts shifting from the confined space towards the well. Slight differences are noted between the pressures generated from the K-value and the ones from the standard method (regardless of presence of oil mobility), this is due to the higher mobility of the hydrocarbon sample in the standard method simulation which comprises a larger vapor phase.

When comparing the pressure profiles of the non-mobile oil sets (Fig.4.18) to the ones that have mobile oil (Fig.4.20), one can notice that the pressure gradient from the edge of the reservoir to the well is much smoother in the cases with mobile oil. The immobile oil in the confined cells acts as an extra barrier to the gas flow and a higher pressure is required to move the gas from the shale matrix towards the fracture network. Hence, in a realistic case, an elevated reservoir pressure and a significant amount of time are required to start draining gas from a shale formation without any external stimulation. In addition, it can be seen in early depletion stages that the amplitude of depletion is larger in standard approach without

confinement effects.

Realization 2: Finer mesh

A second case study was realized again in a two-dimensional setup. This realization has much finer mesh sizes as seen in Fig. 4.15 and the fracture network is not entirely connected to the producer well located on the upper right side.

Similarly to the previous case, the standard methods always overestimate the initial gas saturation in all the cells due to the reduction of the bubble point pressure as seen in Fig.4.24 and Fig.4.22. As expected, the fracture network connected to the producer well drains rapidly in the first 10 days. The surrounding matrix starts experiencing a depletion once the pressure differential is high enough for the gas to shift from the confined pore to the fractures.

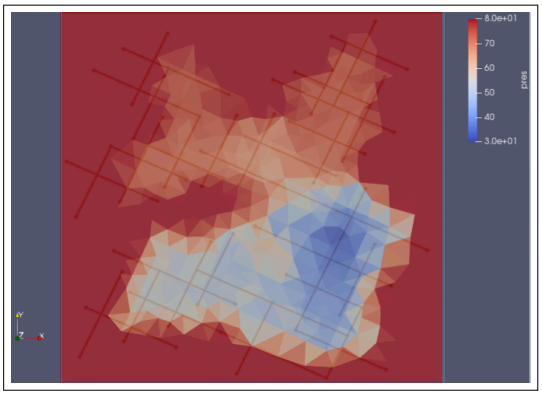

(a) Modified K-Value method at time t= 50 days

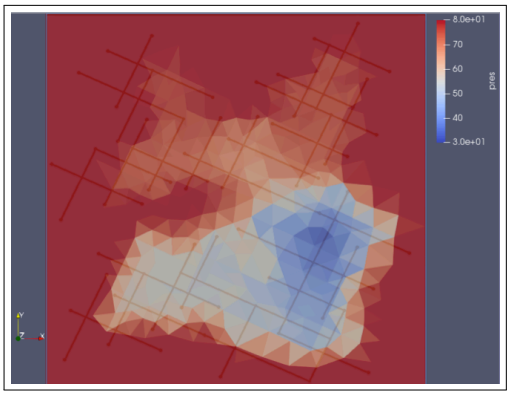

(b) Standard method at time t= 50 days

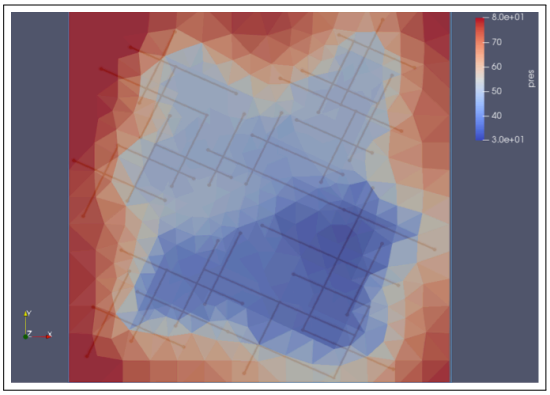

(c) Modified K-Value method t= 200 days

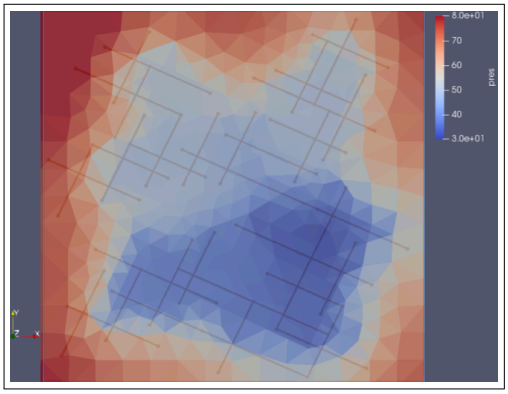

(d) Standard method at time t= 200 days

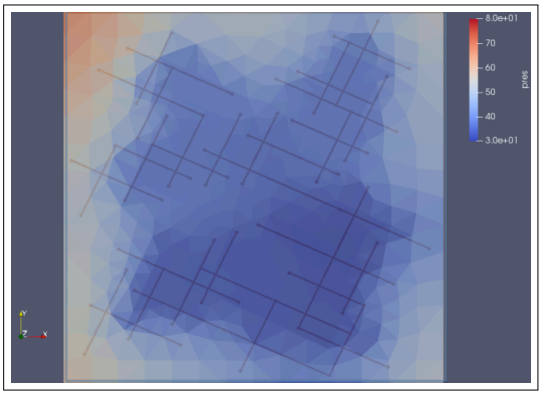

(e) Modified K-Value method at time t= 500 days

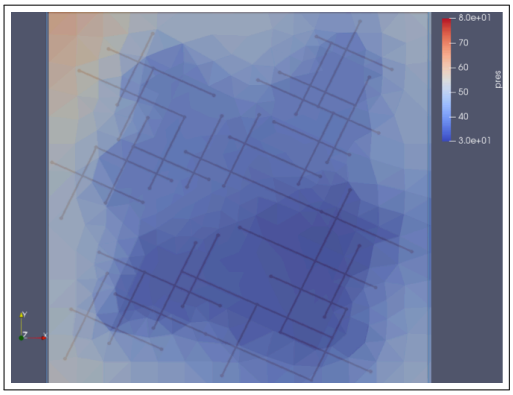

(f) Standard method at time t= 500 days

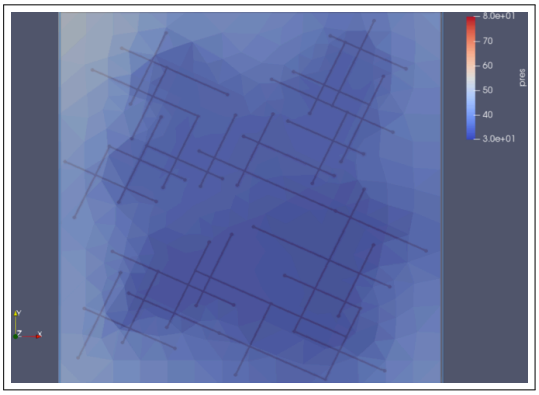

(g) Modified K-Value method at time t= 800 days

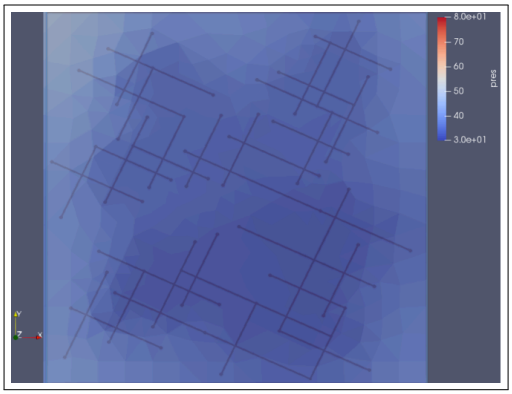

(h) Standard method at time t= 800 days

Figure 4.18: Pressure profiles for modified K-value method and standard method in fractured shale matrix without oil mobility (starting pressure 100 bars)

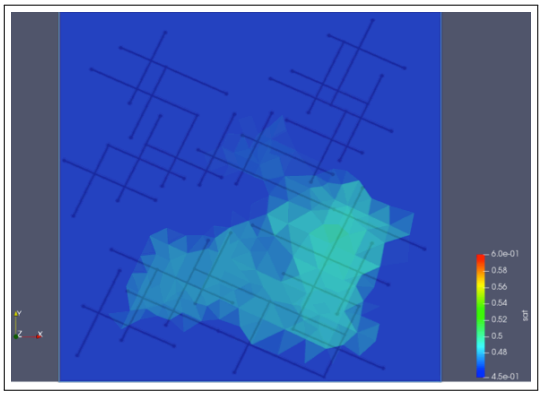

(a) K-value method at time t= 50 days

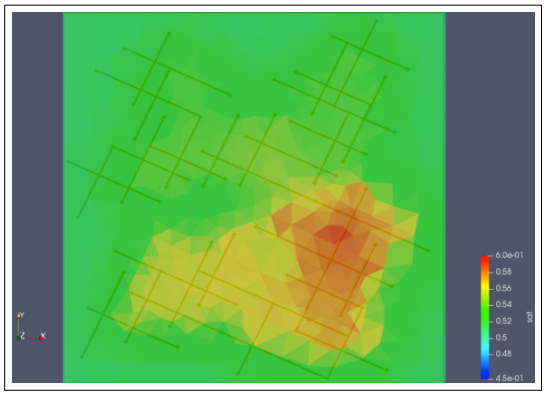

(b) Standard method at time t= 50 days

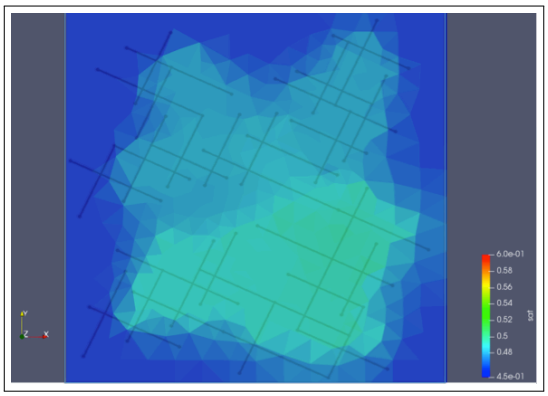

(c) K-value at time t= 200 days

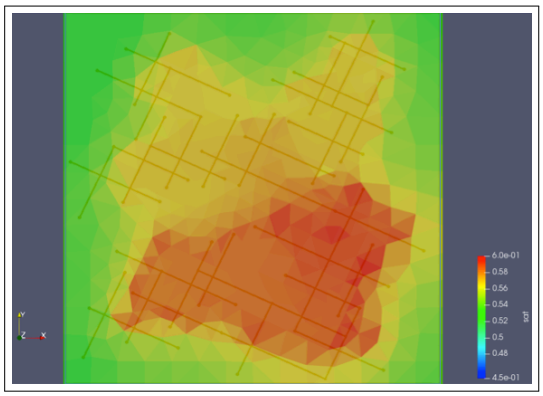

(d) Standard method at time t= 200 days

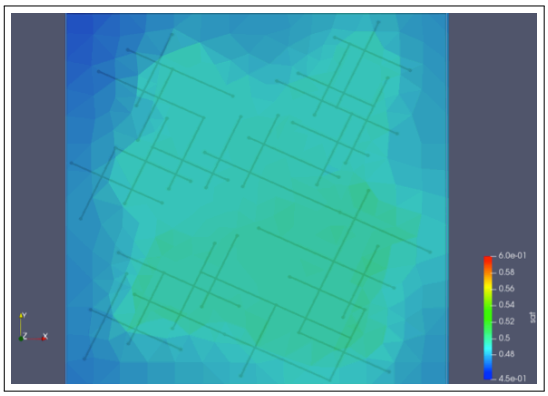

(e) K-value at time t= 500 days

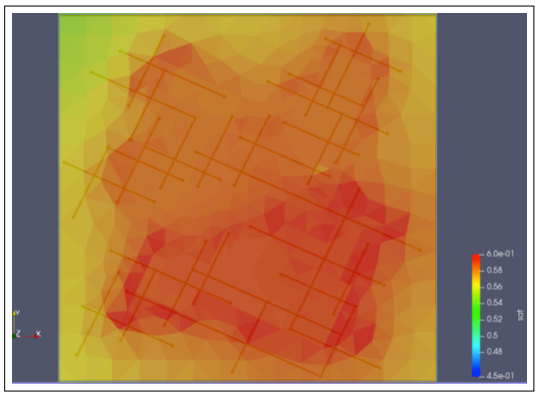

(f) Standard method at time t= 500 days

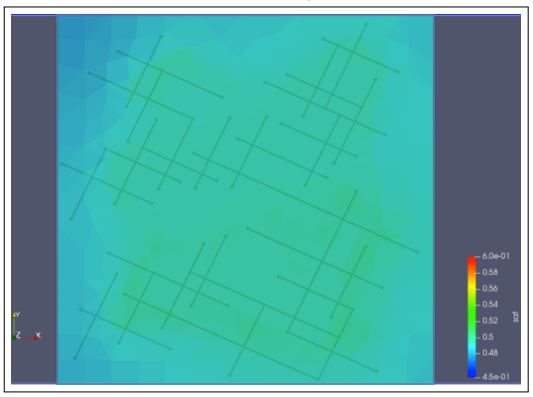

(g) K-value at time t= 800 days

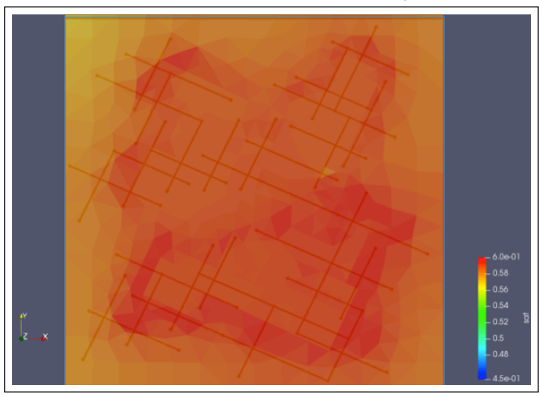

(h) Standard method at time t= 800 days

Figure 4.19: Gas Saturation profiles for modified K-value method and standard simulator in fractured shale matrix without oil mobility (starting pressure 100 bars)

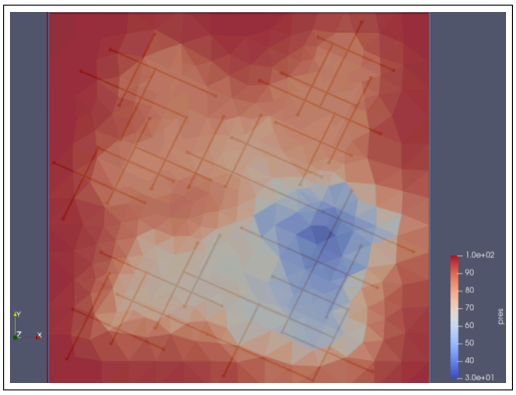

(a) Modified K-Value method at time t= 50 days

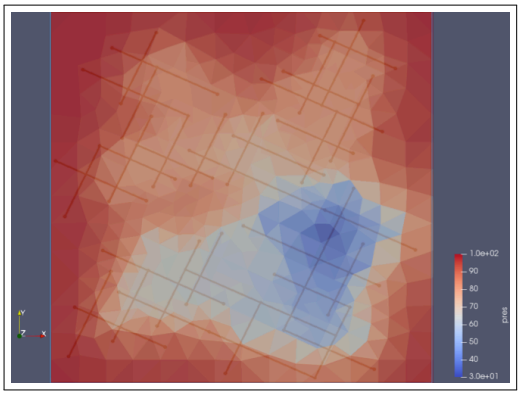

(b) Standard method at time t= 50 days

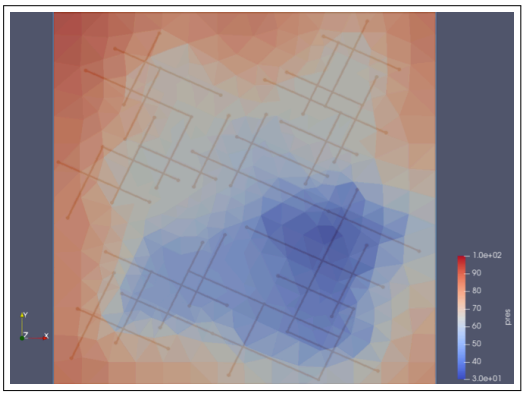

(c) Modified K-Value method t= 200 days

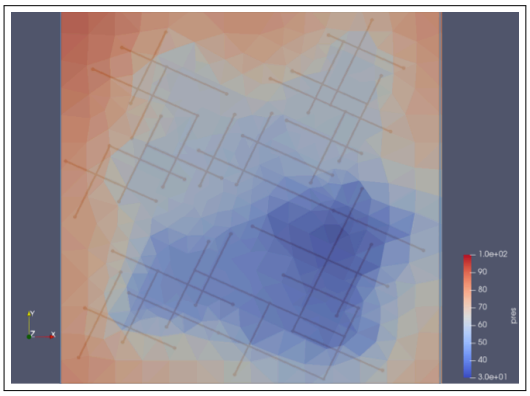

(d) Standard method at time t= 200 days

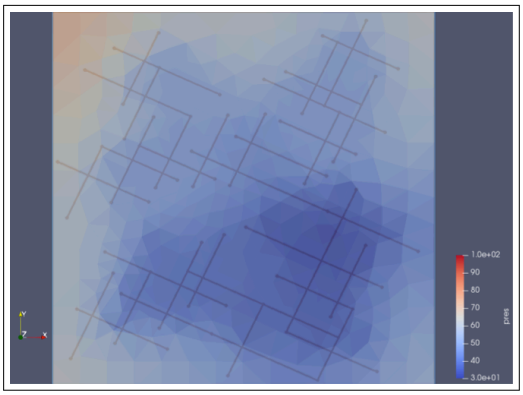

(e) Modified K-Value method at time t= 500 days

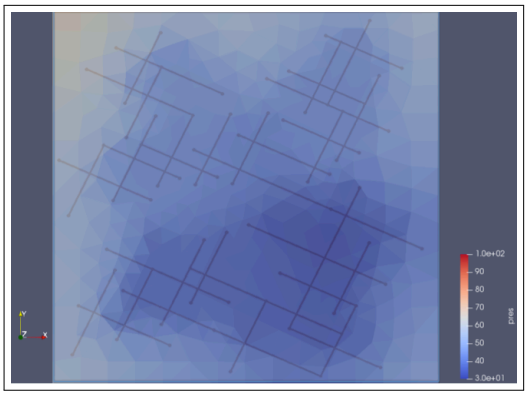

(f) Standard method at time t= 500 days

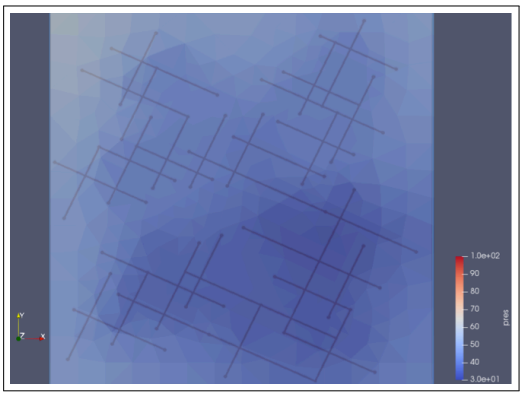

(g) Modified K-Value method at time t= 800 days

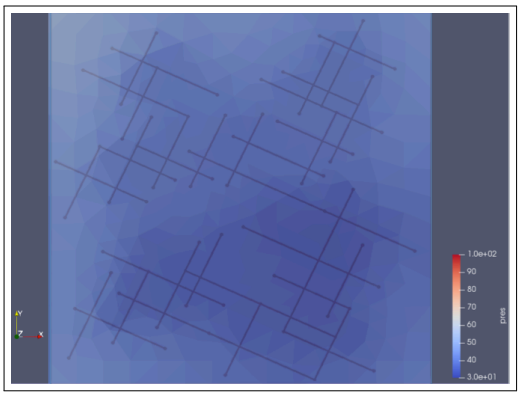

(h) Standard method at time t= 800 days

Figure 4.20: Pressure profiles for modified K-value method and standard method in fractured shale matrix with oil mobility (starting pressure 100 bars)

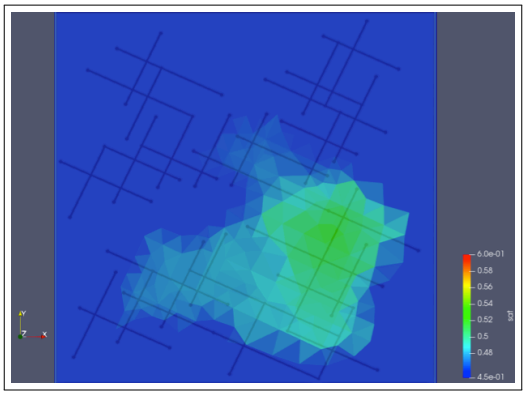

(a) K-value method at time t= 50 days

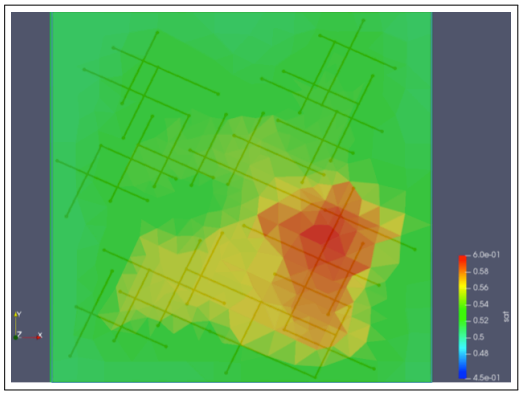

(b) Standard method at time t= 50 days

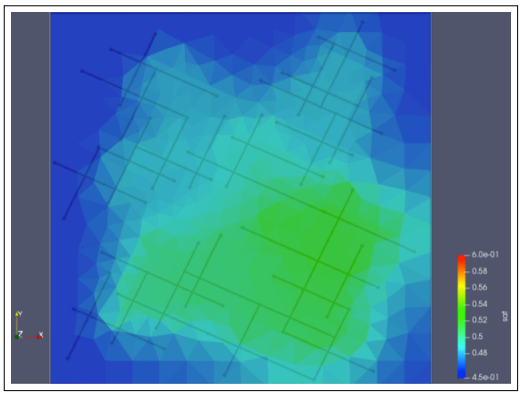

(c) K-value at time t= 200 days

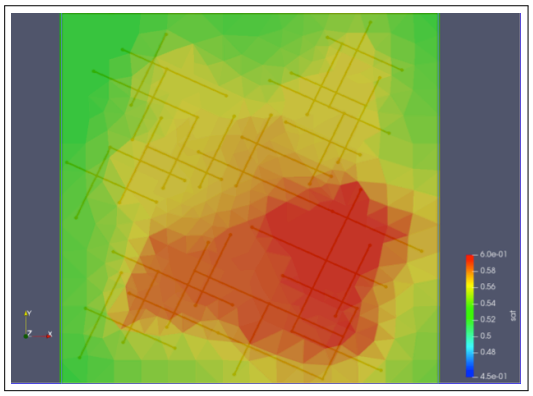

(d) Standard method at time t= 200 days

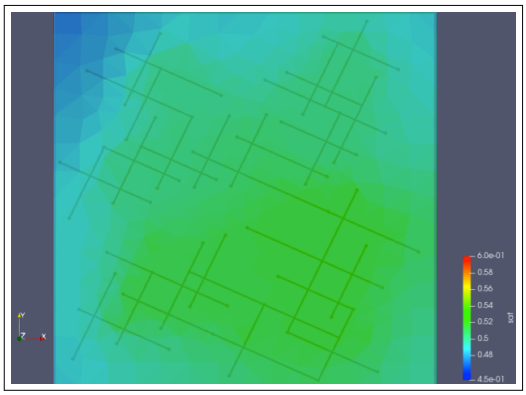

(e) K-value at time t= 500 days

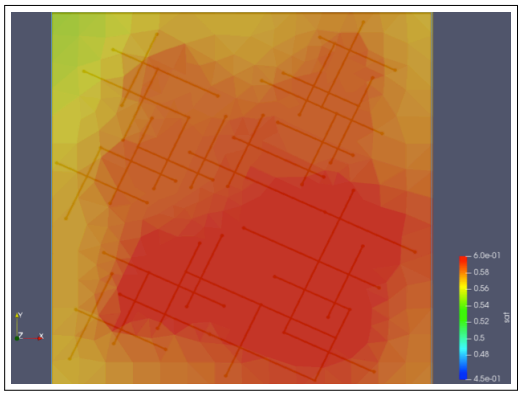

(f) Standard method at time t= 500 days

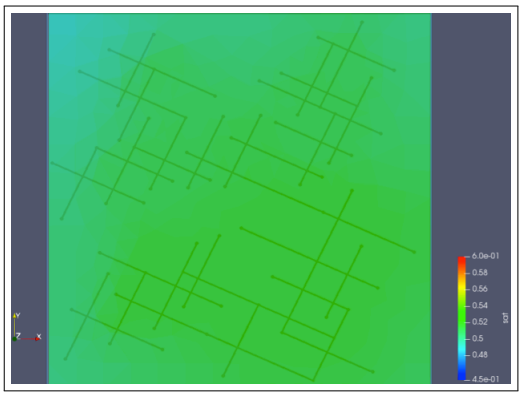

(g) K-value at time t= 800 days

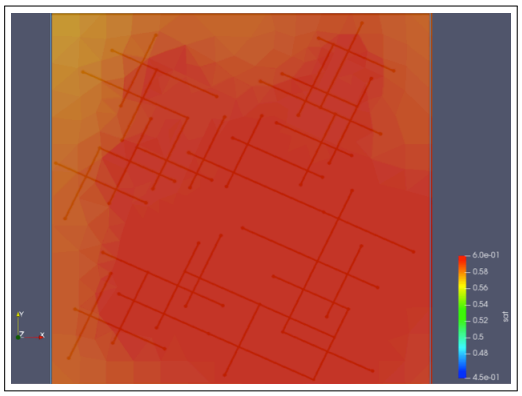

(h) Standard method at time t= 800 days

Figure 4.21: Gas Saturation profiles for modified K-value method and standard simulator in fractured shale matrix with oil mobility (starting pressure 100 bars)

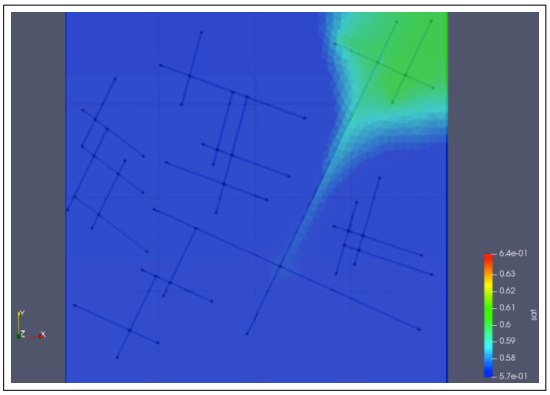

(a) K-value method at time t= 10 days

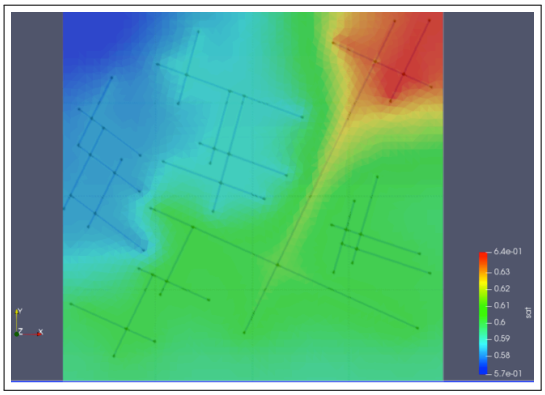

(b) Standard method at time t= 10 days

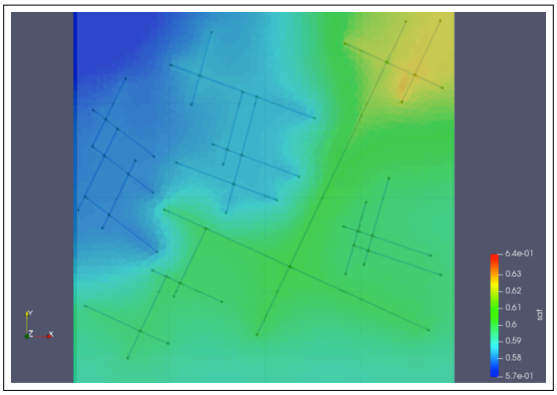

(c) K-value at time t= 20 days

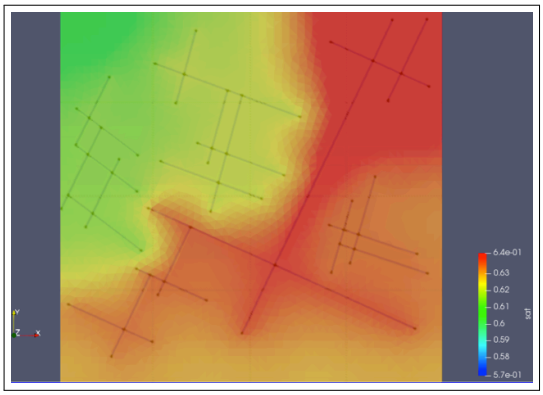

(d) Standard method at time t= 20 days

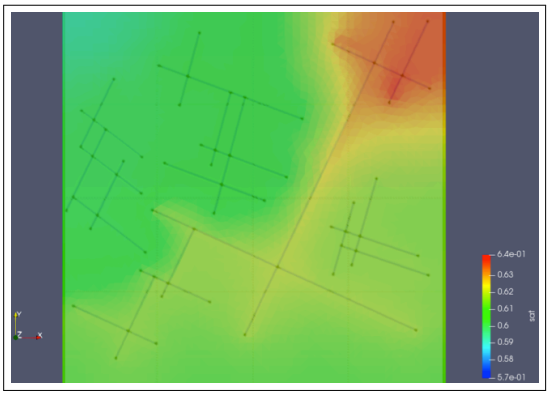

(e) K-value at time t= 30 days

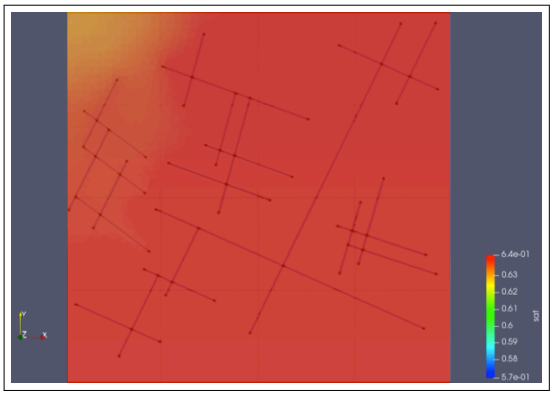

(f) Standard method at time t= 30 days

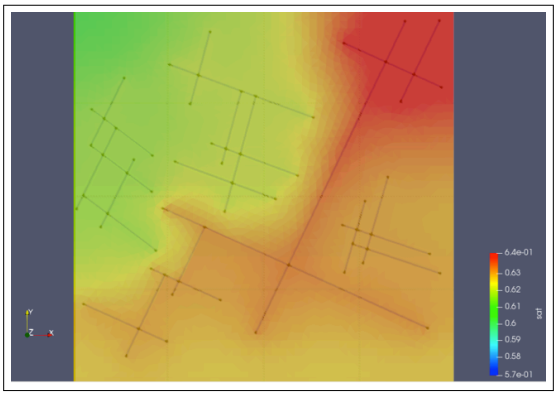

(g) K-value at time t= 40 days

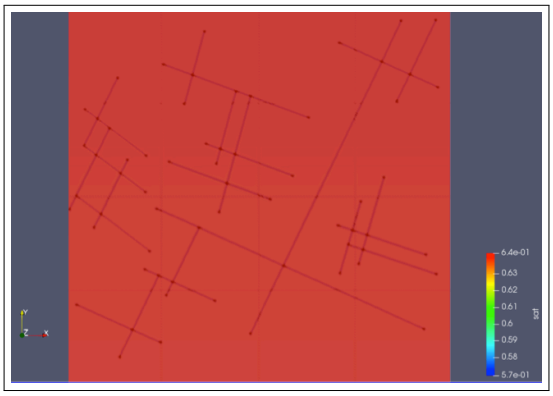

(h) Standard method at time t= 40 days

Figure 4.22: Gas Saturation profiles for modified K-value method and standard simulator in fine fractured shale matrix with oil mobility (starting pressure 100 bars)

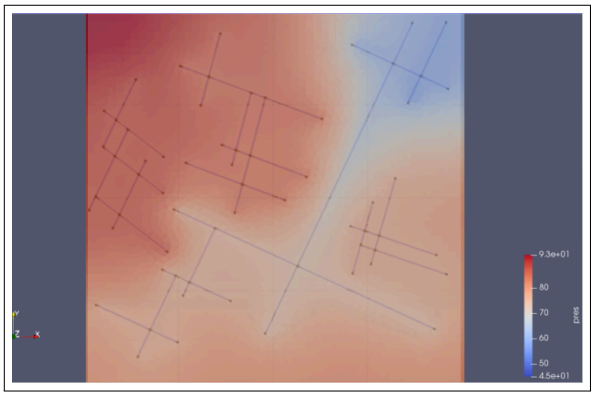

(a) Modified K-Value method at time t= 10 days

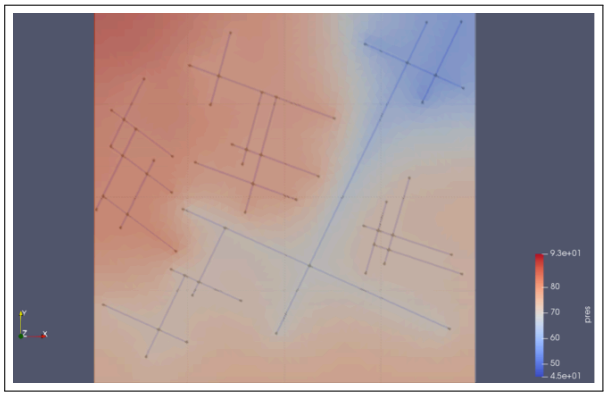

(b) Standard method at time t= 10 days

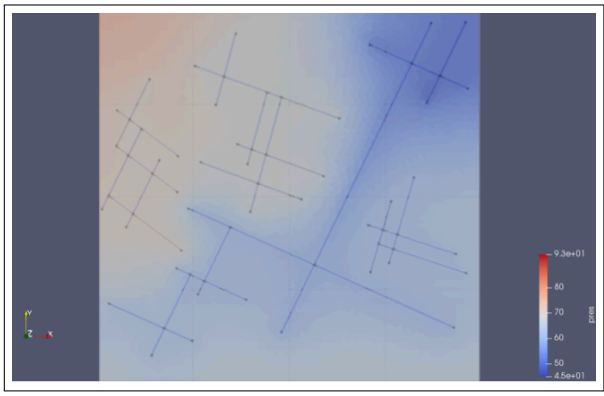

(c) Modified K-Value method t= 20 days

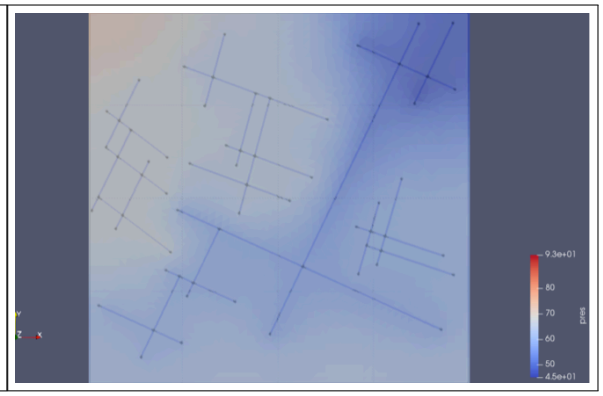

(d) Standard method at time t= 20 days

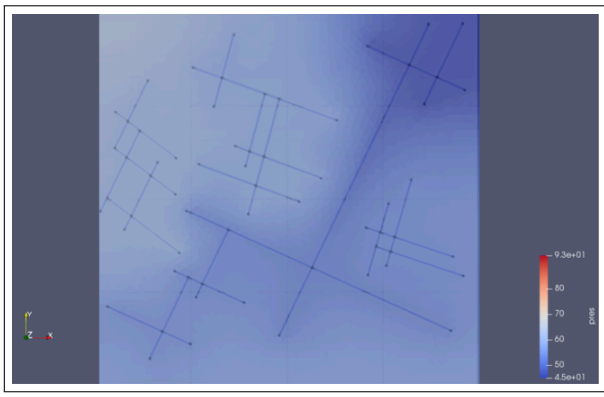

(e) Modified K-Value method at time t= 30 days

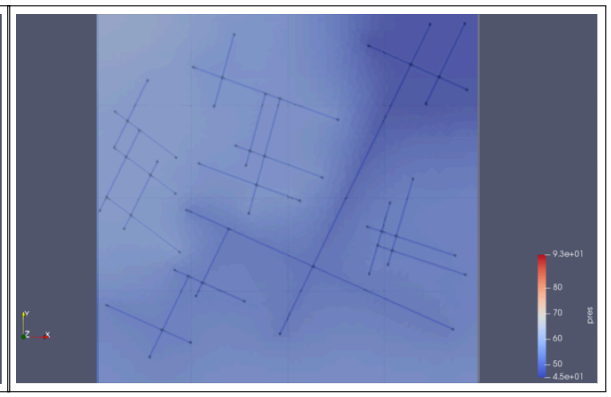

(f) Standard method at time t= 30 days

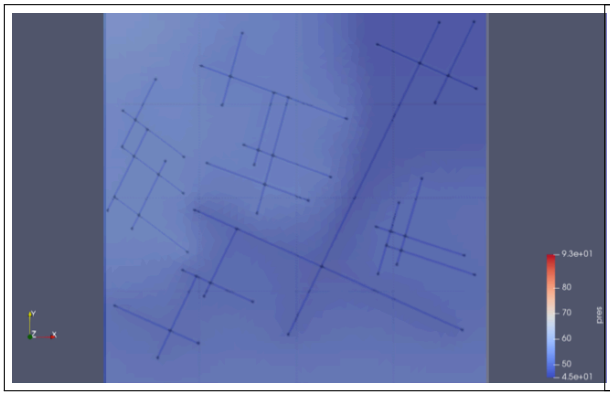

(g) Modified K-Value method at time t= 40 days

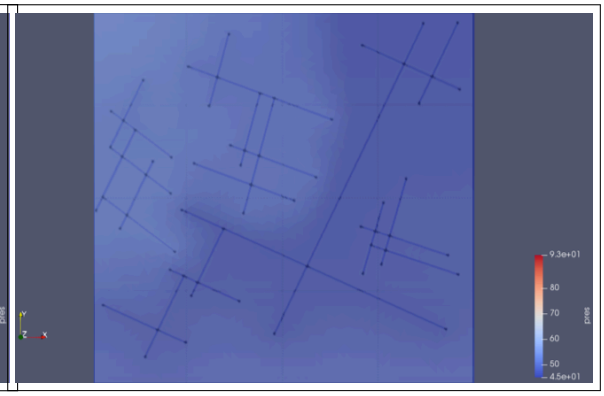

(h) Standard method at time t= 40 days

Figure 4.23: Pressure profiles for modified K-value method and standard method in fine fractured shale matrix with oil mobility (starting pressure 100 bars)

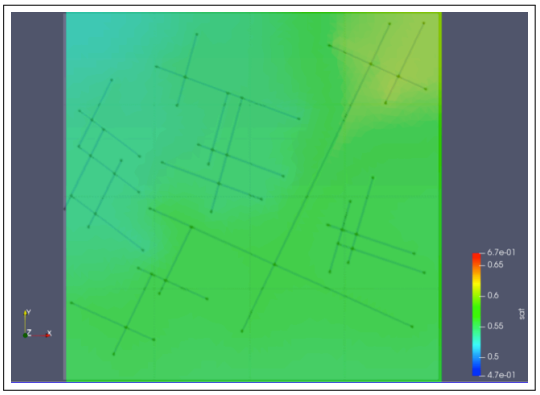

(a) K-value method at time t= 10 days

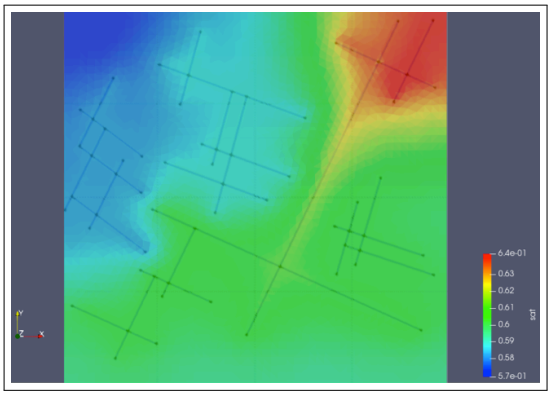

(b) Standard method at time t= 10 days

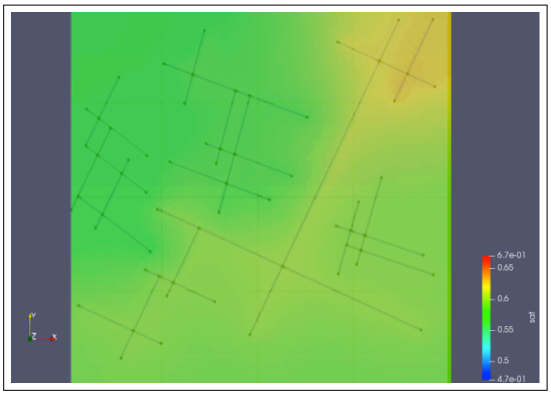

(c) K-value at time t= 20 days

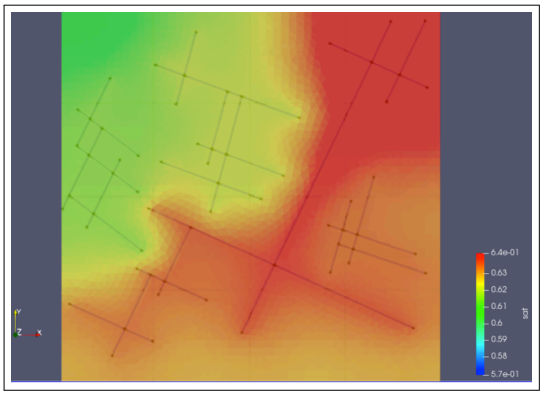

(d) Standard method at time t= 20 days

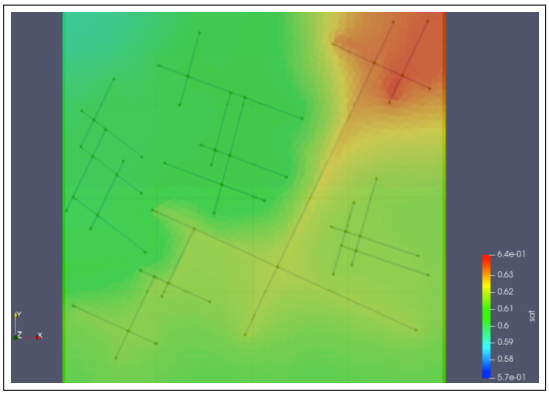

(e) K-value at time t= 30 days

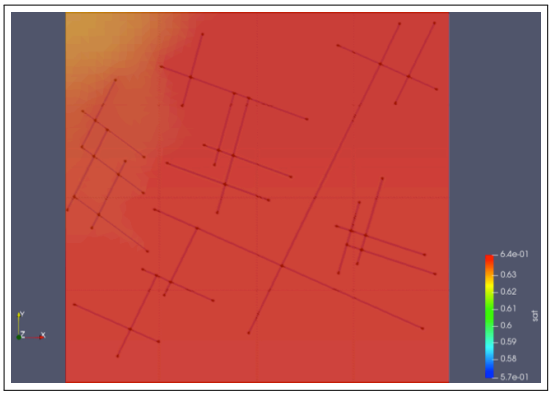

(f) Standard method at time t= 30 days

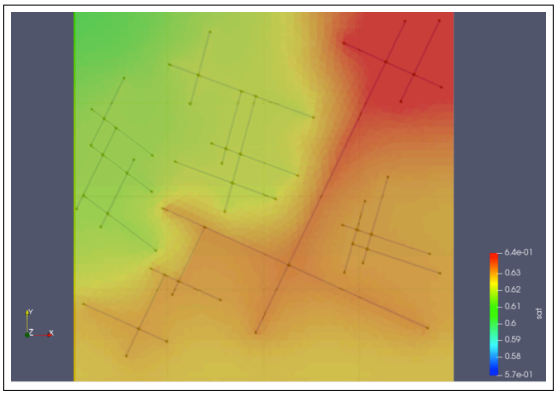

(g) K-value at time t= 40 days

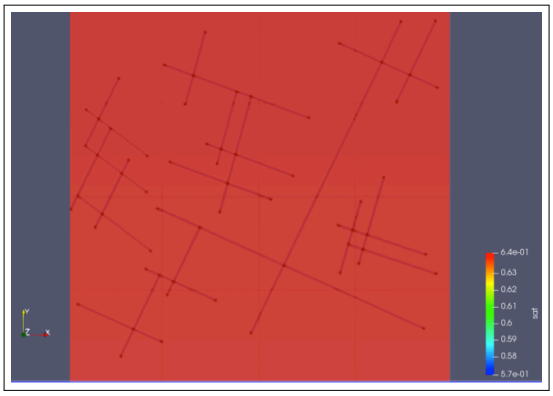

(h) Standard method at time t= 40 days

Figure 4.24: Gas Saturation profiles for modified K-value method and standard simulator in fine fractured shale matrix without oil mobility (starting pressure 100 bars)

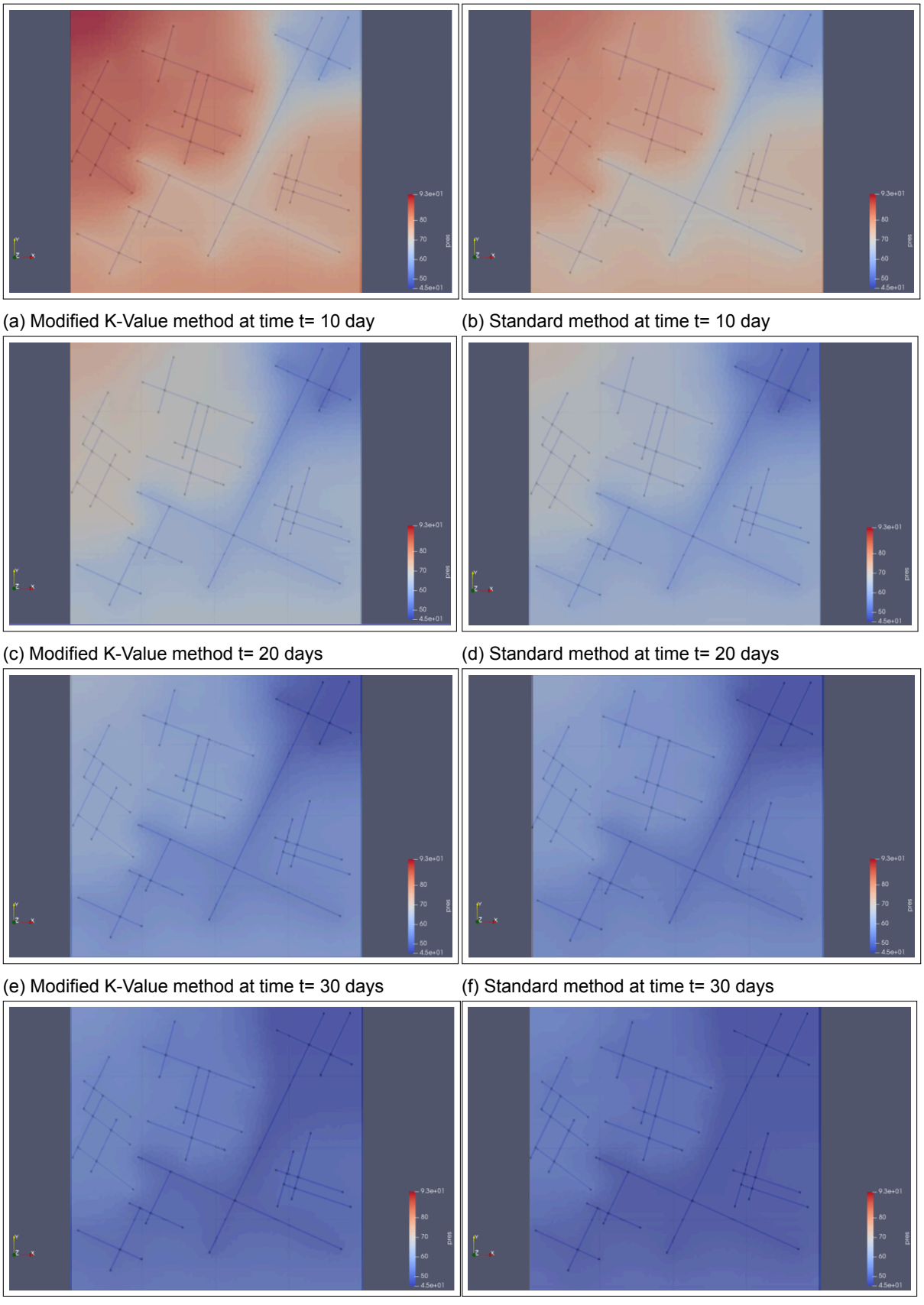

(a) Modified K-Value method at time t= 10 day

(b) Standard method at time t= 10 day

(c) Modified K-Value method t= 20 days

(d) Standard method at time t= 20 days

(e) Modified K-Value method at time t= 30 days

(f) Standard method at time t= 30 days

(g) Modified K-Value method at time t= 40 days

(h) Standard method at time t= 40 days

Figure 4.25: Pressure profiles for modified K-value method and standard method in fine fractured shale matrix without oil mobility (starting pressure 100 bars)

5

Conclusion and Future work

This section summarizes the work explained in the previous chapters and offers suggestions to further develop the project. In chapter 2, a modified K-value has been incorporated to Stanford's Automatic Differentiation General Purpose Research Simulator (ADGPRS). The K-value constraint replaces the equilibrium constraint based on fugacities used in standard compositional simulators. In the proposed K-value approach, we combine equations of state (Peng-Robinson) with the Parachor model and the Laplace equation to include capillary pressure effects to phase behavior computations. The generated K-values are functions of liquid pressure and pore radius. Moreover, a relation was drawn between pore radius and porosity based on gathered field data, in order to link the pore radius factor with the mass balance equations.

In chapter 3, the novel K-value method was successfully validated by comparing it against a compositional model created in Matlab with the capillary pressure term added. The proposed K-value method demonstrated quite accurate results in a simple depletion process.

In chapter 4, several simulations were ran, both in one-dimensional and two-dimensional setups. Analyzing the modified K-value model indicates that capillary pressure effects become significant in pore radii inferior to 100 nanometers and that lower pressure leads to an increase in capillarity. When comparing a homogeneous confined space (2 % porosity) with a non-confined one (20 %), the results of capillary pressure can be noted clearly. The gas production decreased substantially due to the late condensation of the hydrocarbon mixture caused by the bubble point reduction.

The addition of a micro-feature within a confined matrix allows us to study the propagation of gas within a tight shale. At a given pressure and temperature, the gas saturation in a micro-porous space is higher than the surrounding compact formation. As the well is depleted, the excess gas in the feature will migrate straight to the producer well if the latter is connected to the fracture network or it will move slowly within the confined shale towards the producer. The slow migration is due to a very low permeability value associated to the shale, hence the need for artificial reservoir stimulation which can generate an extensive fracture system.

Finally, the depletion of a well in a fractured two-dimensional medium is studied using both a modified K-value method and a standard compositional approach. The latter overestimates the amount of gas generated and isn't entirely reliable to study the production profiles of tight formations. In addition, the stable production from tight formation requires a lower pressure gradient in comparison with the model which does not include confinement effects.

The drawback of the current implementation is that it still relies on Darcy's momentum equation. Unfortunately, little consensus is reached on an accurate model for multiphase flow in tight formations. The consistent model describing multiphase flow in tight porous media is required for an adequate modeling of shale oil production and will be the main topic of our future research.

A

Appendix

A.1. Phase Equilibrium

A.1.1. Gibbs equation

The fundamental thermodynamics equilibrium formulation dictates that the energy applied on a system is dependent on the heat differential over time and work applied on it, as well as the sum of chemical potentials of each component, as seen below:

$$\Delta E = \Delta Q - \Delta W + \sum \mu_i N_i \tag{A.1}$$

Assuming a simple reversible system with no temperature gradient, the fundamental property relation can be rewritten as:

$$dE = TdS - PdV \tag{A.2}$$

Several convenience properties such as enthalpy, Helmhotz energy and Gibbs energy have been developped. The latter is used specifically in phase equilibria where temperature and pressure are controlled. It is defined as:

$$dG = -SdT + VdP \tag{A.3}$$

For phase equilibrium, Gibbs energy is constrained by the fact that its values in both the liquid and vapor phases need to be equal. None of the other thermodynamic values H,S and A need to be equal in both phases.

$$G^L = G^V \tag{A.4}$$

Assuming isothermal conditions ($dT=0$), Gibbs energy is defined as:

$$dG = VdP \tag{A.5}$$

Moreover, at low pressure, we can approximate ideal gas conditions since $Z \simeq 1$ at low pressure. Replacing volume by its equivalent from the ideal gas law, Eqn. 2.14 then turns into:

$$dG = RTZ\frac{dP}{P} \tag{A.6}$$

For an ideal gas, where Z=1, the previous equation can be rewritten as:

$$dG^{ig} = RT\frac{dP}{P} = RTdlnP \tag{A.7}$$

A.1.2. Fugacity

Gibbs equation is used mainly to solve phase equilibrium problems for pure components. For mixtures, an alternative property has been developed as a straightforward extension to Gibbs property, *fugacity*.

Assuming isothermal conditions (dT=0), G.N. Lewis defined fugacity by:

$$dG = RTdlnf \tag{A.8}$$

Fugacity of an ideal gas equals the pressure of the component and the fugacity of a liquid equals its vapor pressure.

The fugacity coefficient, Φ, is also another convenient factor to quantify Gibbs departure. It is defined as:

$$ln\Phi = ln(\frac{f}{P}) = \frac{G - G^{ig}}{RT} \tag{A.9}$$

In equilibrium, Gibbs energy is equivalent in its different phases as mentioned in Eq. 2.13. If we subtract G^{ig} from both sides and divide by RT (again assuming isothermal conditions), we obtain:

$$\frac{G^L - G^{ig}}{RT} = \frac{G^V - G^{ig}}{RT} \tag{A.10}$$

Substituting Eqn. 2.18 into the above yields $ln(\frac{f^L}{P}) = ln(\frac{f^V}{P})$ which becomes:

$$\boxed{f^L = f^V} \tag{A.11}$$

A.2. Development of Jacobian matrix

A.2.1. Derivations of primary equations

Density, volume and fractions are all in molar terms. For example, the volume $V = \frac{V_T}{n}$.

$$F_{p,c} = -\frac{V_i \partial}{\partial t}\Big[\phi(\rho_o S_o x_c + \rho_g S_g y_c)\Big] + \sum_j^n \Big[x_c \rho_o \frac{Kk_{ro}}{\mu_o}\frac{A_{ij}}{l_{ij}}(P_j - P_i) + y_c \rho_g \frac{Kk_{rg}}{\mu_g}\frac{A_{ij}}{l_{ij}}(P_j - P_i)\Big] \tag{A.12}$$

For simplicity, we define the mobility ratio as $\lambda_p = \frac{Kk_{r,p}}{\mu_p}$.

$$\begin{aligned} F_{p,c}^{v+1} = &-\frac{V_i}{\Delta t}\Big[\phi^{v+1}(\rho_o S_o x_c + \rho_g S_g y_c)^{v+1} - \phi^v(\rho_o S_o x_c + \rho_g S_g y_c)^v\Big] \\ &+ \sum_{j=1}^{n}\Big[x_c \rho_o \lambda_o \frac{A_{ij}}{l_{ij}}(P_j - P_i) + y_c \rho_g \lambda_g \frac{A_{ij}}{l_{ij}}[(P + P_{cap})_j - (P + P_{cap})_i]\Big]^{v+1} \end{aligned} \tag{A.13}$$

Deriving with respect to $x_1, x_2 \ldots, x_{N_c}$:

$$\frac{\partial F_{p,c}^{v}}{\partial x_c} = -\frac{V_i}{\Delta t}\left[\phi^v(\rho_o S_o)^v + \phi^v\left(\frac{\partial \rho_o}{\partial x_c} S_o x_c\right)^v\right] + \sum_{j=1}^{n}\left[(P_j - P_i)\frac{A_{ij}}{l_{ij}}[\rho_o \lambda_o + x_c \frac{\partial \rho_o}{\partial x_c}\lambda_o + x_c \frac{\partial \lambda_o}{\partial x_c}\rho_o]\right]^v \quad (A.14)$$

Deriving with respect to $y_1, y_2 \ldots, y_{N_c}$:

$$\frac{\partial F_{p,c}^{v}}{\partial y_c} = -\frac{V_i}{\Delta t}\left[\phi^v(\rho_g S_g)^v + \phi^v\left(\frac{\partial \rho_g}{\partial y_c} S_g y_c\right)^v\right] + \sum_{j=1}^{n}\left[[(P + P_{cap})_j - (P + P_{cap})_i]\frac{A_{ij}}{l_{ij}}[\rho_g \lambda_g + y_c \frac{\partial \rho_g}{\partial y_c}\lambda_g + y_c \frac{\partial \lambda_g}{\partial y_c}\rho_g]\right]^v \quad (A.15)$$

Deriving with respect to S_o:

$$\frac{\partial F_{p,c}^{v}}{\partial S_o} = \sum_{j=1}^{n}\left[x_c \rho_o \frac{\partial \lambda_o}{\partial S_o}\frac{A_{ij}}{l_{ij}}(P_j - P_i) + y_c \rho_g \frac{\partial \lambda_g}{\partial S_o}\frac{A_{ij}}{l_{ij}}[(P + P_{cap})_j - (P + P_{cap})_i]\right]^v - \frac{V_i}{\Delta t}\left[\phi \rho_o x_c\right]^v \quad (A.16)$$

Deriving with respect to S_g:

$$\frac{\partial F_{p,c}^{v}}{\partial S_g} = \sum_{j=1}^{n}\left[x_c \rho_o \frac{\partial \lambda_o}{\partial S_g}\frac{A_{ij}}{l_{ij}}(P_j - P_i) + y_c \rho_g \frac{\partial \lambda_g}{\partial S_g}\frac{A_{ij}}{l_{ij}}[(P + P_{cap})_j - (P + P_{cap})_i]\right]^v - \frac{V_i}{\Delta t}\left[\phi \rho_g y_c\right]^v \quad (A.17)$$

Deriving with respect to S_w:

$$\frac{\partial F_{p,c}^{v}}{\partial S_w} = \sum_{j=1}^{n}\left[x_c \rho_o \frac{\partial \lambda_o}{\partial S_w}\frac{A_{ij}}{l_{ij}}(P_j - P_i) + y_c \rho_g \frac{\partial \lambda_g}{\partial S_w}\frac{A_{ij}}{l_{ij}}[(P + P_{cap})_j - (P + P_{cap})_i]\right]^v \quad (A.18)$$

Deriving with respect to P_i:

$$\frac{\partial F_{p,c}^{v}}{\partial P_i} = -\frac{V_i}{\Delta t}\left[\phi\left(\frac{\partial \rho_g}{\partial P} S_g y_c\right) + \phi\left(\frac{\partial \rho_o}{\partial P} S_o x_c\right)\right]^v + \sum_{j=1}^{n}\left[(P_j - P_i)\frac{A_{ij}}{l_{ij}}[x_c \frac{\partial \rho_o}{\partial P_i}\lambda_o + x_c \frac{\partial \lambda_o}{\partial P_i}\rho_o] - \frac{A_{ij}}{l_{ij}}(x_c \lambda_o \rho_o)\right]^v + \sum_{j=1}^{n}\left[[(P + P_{cap})_j - (P + P_{cap})_i]\frac{A_{ij}}{l_{ij}}[y_c \frac{\partial \rho_g}{\partial P_i}\lambda_g + y_c \frac{\partial \lambda_g}{\partial P_i}\rho_g] - \frac{A_{ij}}{l_{ij}}(y_c \lambda_g \rho_g)\right]^v \quad (A.19)$$

The phase mobility is given by:

$$\lambda_\alpha(S_\alpha, P_i, x_i, y_i) = \frac{K k_{r,\alpha}(S_\alpha)}{\mu_\alpha(P_i, x_i, y_i)} \quad (A.20)$$

The phase relative permeabilities are defined as:

$$k_{r,\alpha}(S_\alpha) = k_{r,\alpha,e}\Big(\frac{S_\alpha - S_{\alpha,r}}{1 - S_{w,c} - S_{o,r}}\Big)^{n_\alpha} \tag{A.21}$$

$$V_\alpha = \frac{V}{n} = \frac{Z_\alpha RT}{P_\alpha} \tag{A.22}$$

$$\frac{\partial V}{\partial P_\alpha} = \frac{\partial Z_\alpha}{\partial P_\alpha}\frac{RT}{P_\alpha} - \frac{Z_\alpha RT}{P_\alpha^2} \tag{A.23}$$

$$\frac{\partial \rho_\alpha}{\partial P_\alpha} = \frac{-1}{V^2}\frac{\partial V}{\partial P_\alpha} \tag{A.24}$$

$$\frac{\partial \rho_\alpha}{\partial z_{i,\alpha}} = \frac{-1}{V^2}\Big(\frac{\partial Z}{\partial z_{i,\alpha}}\frac{RT}{P_\alpha}\Big) \tag{A.25}$$

where $z_{i,\alpha}$ represents the molar fraction of a component i in a specific phase. $z_{i,\alpha} = x_i$ in the liquid phase and $z_{i,\alpha} = y_i$ in the vapor phase. [1]

The Lohrentz-Bray-Clark (LBC) correlation is the most popular viscosity model in the oil industry. It expresses gas and oil viscosities as a fourth degree polynomial in reduced density:

$$\Big[(\mu - \mu^0)\xi_T + 10^(-4)\Big]^{0.25} = a_0 + a_1\rho_{pr} + a_2\rho_{pr}^2 + a_3\rho_{pr}^3 + a_4\rho_{pr}^4 \tag{A.26}$$

where $a_0 = 0.1023, a_1 = 0.023364, a_2 = 0.058533, a_3 = -0.040758 and a_4 = 0.0093324.$

$$\xi_T = 5.35\Big(\frac{T_{pc}}{M^3 P_{pc}^4}\Big) \tag{A.27}$$

$$\rho_{pr} = \frac{\rho}{\rho_{pc}} = \frac{\rho}{M}v_{pc} \tag{A.28}$$

$$\mu^0 = \frac{\sum_{i=1}^{N_c}(z_i\mu_i\sqrt{M_i})}{\sum_{i=1}^{N_c}(z_i\sqrt{M_i})} \tag{A.29}$$

Pseudo-critical properties T_{pc},P_{pc} and v_{pc} are computed using Kay's mixing room, i.e: $P_{pc} = \sum_{i=1}^{N_c} x_i P_{ci}$, $T_{pc} = \sum_{i=1}^{N_c} x_i T_{ci}$ in the liquid phase and $P_{pc} = \sum_{i=1}^{N_c} y_i P_{ci}$, $T_{pc} = \sum_{i=1}^{N_c} y_i T_{ci}$ in the vapor phase.

Viscosities specific for each component, μ_i, can be calculated using Stiel and Thodos correlation.

[1] Do not confuse between Z, the compressibility factor and z, the molar fraction.

A.2.2. Derivations of secondary equations

$$F_{s,i} = K_i x_i - y_i \tag{A.30}$$

$$\frac{\partial F_{s,i}}{\partial x_i} = K_i \tag{A.31}$$

$$\frac{\partial F_{s,i}}{\partial y_i} = -1 \tag{A.32}$$

$$\frac{\partial F_{s,i}}{\partial x_i} = 1 \tag{A.33}$$

$$\frac{\partial F_{s,i}}{\partial S_o} = \frac{\partial F_{s,i}}{\partial S_g} = \frac{\partial F_{s,i}}{\partial S_w} = \frac{\partial F_{s,i}}{\partial P} = 0 \tag{A.34}$$

$$F_s = \sum_{i=1}^{N_c} x_i - 1 \tag{A.35}$$

$$\frac{\partial F_{s,i}}{\partial x_i} = 1 \tag{A.36}$$

$$\frac{\partial F_{s,i}}{\partial S_o} = \frac{\partial F_{s,i}}{\partial S_g} = \frac{\partial F_{s,i}}{\partial S_w} = \frac{\partial F_{s,i}}{\partial P} = \frac{\partial F_{s,i}}{\partial y_i} = 0 \tag{A.37}$$

$$F_s = \sum_{i=1}^{N_c} y_i - 1 \tag{A.38}$$

$$\frac{\partial F_{s,i}}{\partial y_i} = 1 \tag{A.39}$$

$$\frac{\partial F_{s,i}}{\partial S_o} = \frac{\partial F_{s,i}}{\partial S_g} = \frac{\partial F_{s,i}}{\partial S_w} = \frac{\partial F_{s,i}}{\partial P} = \frac{\partial F_{s,i}}{\partial x_i} = 0 \tag{A.40}$$

Bibliography

[1] Raymond Joseph Ambrose, Robert Chad Hartman, Mery Diaz Campos, I Yucel Akkutlu, Carl Sondergeld, et al. New pore-scale considerations for shale gas in place calculations. In *SPE Unconventional Gas Conference*. Society of Petroleum Engineers, 2010.

[2] K. H. Coats. An equation of state compostional model. *SPE Journal*, 20:363–376, 1980.

[3] S Connell-Madore and TJ Katsube. *Pore-size-distribution characteristics of Beaufort-Mackenzie Basin shale samples, Northwest Territories*. Natural Resources Canada, 2006.

[4] Mark E Curtis, Carl H Sondergeld, Raymond J Ambrose, and Chandra S Rai. Microstructural investigation of gas shales in two and three dimensions using nanometer-scale resolution imagingmicrostructure of gas shales. *AAPG bulletin*, 96(4):665–677, 2012.

[5] Sijbren de Jong, Willem Auping, and Joris Govers. *The Geopolitics of Shale Gas: THE IMPLICATIONS OF THE US'SHALE GAS REVOLUTION ON INTRASTATE STABILITY WITHIN TRADITIONAL OIL–AND NATURAL GAS-EXPORTING COUNTRIES IN THE EU NEIGHBORHOOD*. The Hague Centre for Strategic Studies, 2014.

[6] U.S. Energy Information Administration (EIA). Technically recoverable shale oil and shale gas resources: An assessment of 137 shale formations in 41 countries outside the united states. Technical report, U.S. Department of Energy, Washington, DC 20585, June 2013.

[7] C. Geuzaine and J.-F. Remacle. Gmsh: A 3-d finite element mesh generator with built-in pre- and post-processing facilities. *International Journal for Numerical Methods in Engineering*, 79(11):1309–1331, 2009. doi: 10.1002/nme.2579.

[8] Haider and Aziz. Impact of capillary pressure and critical property shift due to confinement on hydrocarbon production in shale reservoirs, August 2015.

[9] Batool Arhamna Haider. *Impact of Capillary Pressure and Critical Properties Shift Due to Confinement on Hydrocarbon Production from Shale Reservoirs*. PhD thesis, Stanford University, 2015.

[10] Utpalendu Kuila and Manika Prasad. Specific surface area and pore-size distribution in clays and shales. *Geophysical Prospecting*, 61(2):341–362, 2013.

[11] Robert G Loucks, Robert M Reed, Stephen C Ruppel, and Daniel M Jarvie. Morphology, genesis, and distribution of nanometer-scale pores in siliceous mudstones of the mississippian barnett shale. *Journal of sedimentary research*, 79(12):848–861, 2009.

[12] Qingmin Meng. The impacts of fracking on the environment: A total environmental study paradigm. *Science of The Total Environment*, 580:953–957, 2017.

[13] Rasoul Nazari Moghaddam and Mahmoud Jamiolahmady. Slip flow in porous media. *Fuel*, 173:298–310, 2016.

[14] Philip H Nelson. Pore-throat sizes in sandstones, tight sandstones, and shales. *AAPG bulletin*, 93(3):329–340, 2009.

[15] Bahareh Nojabaei, Russell T Johns, Lifu Chu, et al. Effect of capillary pressure on phase behavior in tight rocks and shales. *SPE Reservoir Evaluation & Engineering*, 16 (03):281–289, 2013.

[16] Jianyuan Pang, Julian Youxiang Zuo, Dan Zhang, Liangui Du, et al. Impact of porous media on saturation pressures of gas and oil in tight reservoirs. In *SPE Canadian Unconventional Resources Conference*. Society of Petroleum Engineers, 2012.

[17] Frédéric Pouchot. Shale gas, oil reshape world energy landscape, 2013. URL `https://phys.org/news/2013-09-shale-gas-oil-reshape-world.html`.

[18] Roger M Slatt and Neal R O'Brien. Pore types in the barnett and woodford gas shales: Contribution to understanding gas storage and migration pathways in fine-grained rocks. *AAPG bulletin*, 95(12):2017–2030, 2011.

[19] Sugata P Tan and Mohammad Piri. Equation-of-state modeling of confined-fluid phase equilibria in nanopores. *Fluid Phase Equilibria*, 393:48–63, 2015.

[20] Cong Wang. *Pressure transient analysis of fractured wells in shale reservoirs*. Colorado School of Mines, 2013.

[21] Wei Yu, Kamy Sepehrnoori, Tadeusz Wiktor Patzek, et al. Evaluation of gas adsorption in marcellus shale. In *SPE Annual Technical Conference and Exhibition*. Society of Petroleum Engineers, 2014.